J. Fluid Mech. (1991), *vol.* 226, *pp.* 257–289
Printed in Great Britain

Vorticity dynamics in an oscillatory flow over a rippled bed

By P. BLONDEAUX AND G. VITTORI
Hydraulic Institute, University of Genoa, Via Montallegro, 1, 16145 Genoa, Italy

(Received 9 March 1990 and in revised form 31 October 1990)

In the present paper we determine the oscillatory flow generated by surface gravity waves near a sea bottom covered with large-amplitude ripples. The vorticity equation and Poisson equation for the stream function are solved by means of a numerical approach based on spectral methods and finite-difference approximations. In order to test the numerical algorithm and in particular the numerical scheme used to generate vorticity along the ripple profile, we also perform an asymptotic analysis, which holds as the time t tends to zero. The main features of the time development of vorticity are analysed and particular attention is paid to the dynamics of the large vortices generated by flow separation at the ripple crests and along the ripple profile. Some of the results obtained by Longuet-Higgins (1981) are recovered; in particular, the present results show a vortex pair shed from the ripple crest every half-cycle. The determination of flow separation along the ripple profile induced by the pressure gradient and the inclusion of viscous effects allows us to obtain accurate quantitative results and detect some important phenomena never observed before.

In particular it is shown that: (i) Whenever a vortex structure moves towards the bottom, a secondary vortex is generated near the ripple profile, which interacts with the primary vortex and causes it to move away from the bottom. (ii) Depending on the values of the parameters, the time development of the free shear layer shed from the ripple crest may produce two or even more vortex structures. (iii) Occasionally vortices generated previously may coalesce with the free shear layer shed from the ripple crest, generating a unique vortex structure.

1. Introduction

The purely horizontal back-and-forth motion produced near a cohesionless bed by progressive gravity waves propagating in shallow water usually gives rise to nearly symmetrical bedforms commonly known as ripples.

Even though it was recognized as early as Ayrton (1910) that the formation of sand ripples is connected with the existence of vortices shed at the crests of the ripples in alternate directions every half-cycle, detailed quantitative knowledge of the vorticity dynamics is still lacking. There have been many experimental studies of the velocity distribution close to a rippled bed in oscillatory flow (Nakato *et al.* 1977; Du Toit & Sleath 1981; Sato, Shimosaka & Watanabe 1987; Ikeda *et al.* 1989). However, results reported in the literature are mainly concerned with velocity measurements on a coarse grid close to the bed and do not provide an overall picture of the time development of the vorticity field. A detailed knowledge of the dynamics of the vortex structures generated by flow separation at the ripple crests is necessary in order to understand important phenomena which take place near the bottom and in

particular the mechanism through which sediment grains are lifted up and maintained in suspension.

The experimental evidence (Nielsen 1979; Sunamura 1980) suggests that in a wave cycle two distinct mechanisms operate. The first is the trapping of sediment in the vortex structures which are generated by flow separation at the ripple crests. When flow reverses and the vortex structures are no longer reinforced but simply convected by the local velocity, the second mechanism operates: sediment is carried in suspension far from the point where it was picked up and then is slowly released when vortices decay because of viscous effects. A model to transform these qualitative observations into quantitative results has not yet been formulated.

In order to overcome the above difficulties Sleath (1973) and Sato, Mimura & Watanabe (1984) carried out numerical calculations of the oscillatory flow over a wavy bed. They assumed the flow to be two-dimensional and solved numerically the vorticity equation and Poisson equation for the stream function by a finite-difference scheme. The above numerical method fails when applied to conditions characterized by the relatively large values of the Reynolds number characteristic of the flow at the bottom of gravity waves. In fact a large number of grid points is necessary in order to describe both the irrotational part of the flow and the boundary layer adjacent to the bottom, and consequently an extremely large amount of CPU time would be required.

Longuet-Higgins (1981) tried to overcome the above difficulties by assuming that the flow can be represented by the superposition of an oscillatory irrotational component over the wavy wall and of the flow induced by a vortex sheet generated by flow separation at the ripple crest. The evolution of the vortex sheet is then computed through its representation in terms of a finite number of point vortices. However, as pointed out by Sleath (1984), the latter method presents some drawbacks. In fact, though Longuet-Higgins (1981) did incorporate some viscous effects, the discrete vortex method is essentially inviscid. In other words it is assumed that viscous boundary layers remain thin and passive for all times except at singular geometrical points where they separate and generate a vortex sheet. Whence, if applied to the oscillatory flow over a rippled bed, a discrete vortex method fails to provide quantitative results when the boundary-layer thickness is of the same order of magnitude as ripple height and when flow separation is induced along the flat ripple profile.

A study of the viscous oscillatory flow over a rippled bed has also been performed by Smith & Stansby (1985) by means of a vortex-in-cell method (Christiansen 1973). In this method the vorticity field is discretized into a set of vortices which are created on the ripple profile to satisfy the no-slip condition and convected in an inviscid calculation; moreover, random walks are imposed to simulate the process of viscous diffusion. The above authors have recently successfully applied the vortex-in-cell method to compute the impulsively started flow around a circular cylinder (Smith & Stansby 1988). However, in the case of the oscillatory flow over a rippled bed, vortices are not convected far away from generation points, whence the authors were forced to introduce an empirical time decay of vorticity which makes the approach less rigorous. Moreover Smith & Stansby (1985) did not perform a systematic investigation of flow characteristics as functions of the various physical parameters of the problem.

Numerical studies of the oscillatory flow over a wavy wall were also performed, among others, by Ralph (1986, 1988) and Sobey (1980, 1982, 1983). However, these works were mainly aimed at the study of the dynamics of physiological flows and

they focused attention only on internal flows with wall waviness characterized by a scale of the same order of magnitude as the characteristic viscous length. As a consequence results described in Ralph (1986, 1988) and Sobey (1980, 1982, 1983) cannot be used to obtain even qualitative informations on oscillatory flow at the bottom of sea waves where the constraints present in internal flows are absent and ripples are characterized by wavelengths much larger than the bottom boundary-layer thickness.

In the present paper we determine the flow field close to a sea bottom covered with ripples. We attempt to overcome the difficulties described previously by employing a numerical approach based on spectral methods and finite-difference approximations which allows us to obtain detailed results in a range of parameters of physical relevance by means of a limited amount of CPU time.

In particular the numerical approach is able to describe both the irrotational part of the flow and viscous boundary layers for relatively large values of the Reynolds number. Thus the dynamics of the vortices generated by flow separation at the ripple crests is analysed along with the dynamics of the vortex structures generated by flow separation along the ripple profile induced by pressure gradients. Some of the results obtained by Longuet-Higgins (1981) are thus recovered. In particular the present results show a vortex pair shed from the ripple crest every half-cycle. The inclusion of viscous effects allows us to obtain accurate quantitative results and detect some new interesting phenomena:

(i) Whenever a vortex structure moves towards the bottom, a cell of recirculating flow appears underneath the vortex. This recirculating cell is then ejected into the inviscid region leaving behind a free shear layer which rolls up into a strong secondary vortex which interacts with the primary vortex and causes it to move away from the bottom. This mechanism originates vortex pairs which were not detected previously.

(ii) Depending on the values of the parameters, the evolution of the free shear layer originated by flow separation at the ripple crest may produce two or even more vortex structures which develop independently of each other.

(iii) Occasionally vortices generated previously come into close contact with the free shear layer shed from the ripple crest and coalesce with the latter generating a unique vortex structure.

These phenomena cause the flow field to assume rapidly a complex behaviour which requires suitable averages to be performed in order to gain a clear picture of the process.

In the next section we formulate the problem. The numerical approach is described in §3 while results are presented in §5. In §4 an asymptotic analysis, which holds for small times, is presented and used as a check of the numerical model.

2. Formulation of the problem

Let us consider a two-dimensional gravity wave of small height H^*, length L^* and period T^* in shallow water of depth D^* propagating over a wavy bottom. Let us denote by ρ and ν water density and kinematic viscosity respectively.

It is well established that the flow can be modelled as irrotational except within the unsteady boundary layers adjacent to the bottom and to the free surface. Since we are interested in the interaction between fluid and bottom, we focus our attention on the former layer and use linear wave theory to describe the motion outside this region. We assume the characteristic thickness of the bottom boundary layer to be

much smaller than both the water depth and the length of the gravity wave. Flow in the bottom boundary layer can then be considered as caused by fluid oscillations which are only parametrically dependent on the longitudinal coordinate. We define a Cartesian orthogonal coordinate system (x^*, y^*) with the x^*-axis lying on the bottom and parallel to the direction of wave propagation, the y^*-axis directed upward. The above assumptions allow us to assume the following form for the velocity vector (U^*, V^*) outside the bottom layer:

$$(U^*, V^*) = \left[U_0^* \sin\left(\frac{2\pi t^*}{T^*}\right), 0\right], \tag{1}$$

where t^* is time and U_0^* is the amplitude of the irrotational velocity oscillations evaluated at the bottom.

When the bottom is flat and the flow is laminar, fluid motion is described by the well known Stokes' (1851) solution. The order of magnitude of the boundary-layer thickness is then provided by the quantity

$$\delta^* = (\nu T^*/\pi)^{\frac{1}{2}}.$$

Let us consider a wavy bottom profile $y^* = F(x^*)$ described by the following equations (Sleath 1984):

$$y^* = \tfrac{1}{2}h^* \cos k^* \xi^*; \quad x^* = \xi^* - \tfrac{1}{2}h^* \sin k^* \xi^*, \tag{2a,b}$$

where $k^* = 2\pi/l^*$ is the wavenumber of the bottom profile, h^* is height, and ξ^* is a dummy variable. As observed in real ripples the bed profile (2a, b) exhibits crests sharper than troughs. A comparison between experimental profiles and (2) is performed in Sleath (1984) and shows a good agreement.

Assuming the flow to be two-dimensional, the differential problem governing the flow field is posed by the vorticity equation along with the relationship between the stream function (ψ^*) and the vorticity (ω^*) and boundary conditions which force no slip at the bottom and matching of the inner flow with the outer irrotational motion. Let us introduce the following dimensionless variables:

$$\left.\begin{aligned} t &= \frac{t^* 2\pi}{T^*}, \quad (x, y) = \frac{(x^*, y^*)}{\delta^*}, \quad \psi = \frac{\psi^*}{U_0^* \delta^*}, \\ \omega &= \frac{\omega^* \delta^*}{U_0^*}, \quad (l, h) = \frac{(l^*, h^*)}{\delta^*}, \quad k = k^* \delta^*. \end{aligned}\right\} \tag{3}$$

Then the governing differential problem reads

$$\frac{2}{R_\delta}\frac{\partial \omega}{\partial t} + \frac{\partial \psi}{\partial y}\frac{\partial \omega}{\partial x} - \frac{\partial \psi}{\partial x}\frac{\partial \omega}{\partial y} = \frac{1}{R_\delta}\left[\frac{\partial^2 \omega}{\partial x^2} + \frac{\partial^2 \omega}{\partial y^2}\right], \tag{4}$$

$$\frac{\partial^2 \psi}{\partial x^2} + \frac{\partial^2 \psi}{\partial y^2} = -\omega, \tag{5}$$

$$\frac{\partial \psi}{\partial x} = \frac{\partial \psi}{\partial y} = 0 \quad \text{at} \quad y = F(x), \tag{6a,b}$$

$$\frac{\partial \psi}{\partial x} \to 0, \quad \frac{\partial \psi}{\partial y} \to \sin(t) \quad \text{for} \quad y \to \infty, \tag{7a,b}$$

where R_δ is the Reynolds number of the bottom boundary layer defined as $R_\delta = U_0^* \delta^*/\nu$.

In order to solve the differential system (4)–(7) it is useful to introduce a new orthogonal coordinate system (ξ, η), defined by the following relationships (Sleath 1973):

$$\xi = x + \tfrac{1}{2}h\,\mathrm{e}^{-k\eta}\sin k\xi, \quad \eta = y - \tfrac{1}{2}h\,\mathrm{e}^{-k\eta}\cos k\xi \tag{8a,b}$$

which map the bottom profile into the line $\eta = 0$.

Substitution of (8) into (4)–(7) leads to the following partial differential problem:

$$\frac{\partial\omega}{\partial t} + \frac{R_\delta}{2J}\left[\frac{\partial\psi}{\partial\eta}\frac{\partial\omega}{\partial\xi} - \frac{\partial\psi}{\partial\xi}\frac{\partial\omega}{\partial\eta}\right] = \frac{1}{2J}\left[\frac{\partial^2\omega}{\partial\xi^2} + \frac{\partial^2\omega}{\partial\eta^2}\right], \tag{9}$$

$$\frac{\partial^2\psi}{\partial\xi^2} + \frac{\partial^2\psi}{\partial\eta^2} = -J\omega, \tag{10}$$

$$\frac{\partial\psi}{\partial\xi} = \frac{\partial\psi}{\partial\eta} = 0 \quad \text{at} \quad \eta = 0, \tag{11a,b}$$

$$\frac{\partial\psi}{\partial\xi} \to 0, \quad \frac{\partial\psi}{\partial\eta} \to \sin(t) \quad \text{for} \quad \eta \to \infty, \tag{12a,b}$$

where J is the Jacobian of transformation 8(a,b):

$$J = 1 + \tfrac{1}{4}h^2k^2\,\mathrm{e}^{-2k\eta} - hk\,\mathrm{e}^{-k\eta}\cos k\xi. \tag{13}$$

3. The numerical approach

The problem formulated in §2 is solved numerically following a procedure which makes use of spectral methods and finite-difference approximations.

First we consider the values assumed within a wavelength by the stream function $\psi(\xi, \eta, t)$, the vorticity $\omega(\xi, \eta, t)$ as well as the Jacobian $J(\xi, \eta)$ on a regular grid along the ξ-direction:

$$\left.\begin{aligned} \psi_j(\eta, t) &= \psi\left(\frac{jl}{N}, \eta, t\right), \\ \omega_j(\eta, t) &= \omega\left(\frac{jl}{N}, \eta, t\right), \\ J_j(\eta) &= J\left(\frac{jl}{N}, \eta\right), \end{aligned}\right\} \quad j = 1, 2, \ldots, N. \tag{14}$$

Then the discrete Fourier coefficients are introduced (Orszag 1971)

$$\left.\begin{aligned} \psi_j(\eta, t) &= \sum_{n=0}^{N-1} \Psi_n(\eta, t)\,\mathrm{e}^{\mathrm{i}2\pi n(j/N)}, \\ \omega_j(\eta, t) &= \sum_{n=0}^{N-1} \Omega_n(\eta, t)\,\mathrm{e}^{\mathrm{i}2\pi n(j/N)}, \\ J_j(\eta) &= \sum_{n=0}^{N-1} \mathscr{J}_n(\eta)\,\mathrm{e}^{\mathrm{i}2\pi n(j/N)}, \end{aligned}\right\} \quad j = 1, 2, \ldots, N. \tag{15}$$

Making use of (14), (15) equations (9), (10) are reduced to the following form:

$$\frac{\partial \Omega_n}{\partial t} = -\tfrac{1}{2}R_\delta \mathcal{N}\left\{\left(\frac{1}{\mathscr{J}}\right)_n ; \mathrm{i}\left[\mathcal{N}\left\{\frac{\partial \Psi_n}{\partial \eta}; nk\Omega_n\right\} - \mathcal{N}\left\{nk\Psi_n ; \frac{\partial \Omega_n}{\partial \eta}\right\}\right]\right\}$$

$$+\tfrac{1}{2}\mathcal{N}\left\{\left(\frac{1}{\mathscr{J}}\right)_n ; -n^2k^2\Omega_n + \frac{\partial^2 \Omega_n}{\partial \eta^2}\right\}, \quad n = 0, 1, \ldots, N-1, \tag{16}$$

$$\frac{\partial^2 \Psi_n}{\partial \eta^2} - \eta^2 k^2 \Psi_n = -\mathcal{N}\{\mathscr{J}_n ; \Omega_n\}, \quad n = 0, 1, \ldots, N-1, \tag{17}$$

where the operator $\mathcal{N}\{\ ;\ \}$ is defined by

$$\mathcal{N}\{F_n ; G_n\} = \sum_{m=0}^{2N-1} \tilde{F}_m \tilde{G}_{n-m}, \tag{18}$$

with

$$\tilde{F}_n = F_n \quad \text{for} \quad 0 \leqslant n \leqslant \tfrac{1}{2}N-1,$$

$$\tilde{F}_n = F_{n-N} \quad \text{for} \quad \tfrac{3}{2}N+1 \leqslant n \leqslant 2N-1,$$

$$\tilde{F}_n = 0 \quad \text{otherwise.}$$

The operator $\mathcal{N}$ defined by (18) can be treated as an ordinary convolution sum by appending zeros to the arrays to convolve (Rinaldo & Giorgini 1984). The latter procedure is introduced in order to avoid alaising errors (Orszag 1971).

The reduction of the system (9), (10) to the system (16), (17) transforms the mathematical problem into a time-dependent boundary-value problem in the variable η which is amenable to a classic computational approach.

The solution starts with the establishment of initial conditions for the complex fields Ψ_n, Ω_n which are assumed to vanish. Then the computational cycle begins by implementation of finite-difference equations analogous to the partial differential equations for the discrete Fourier coefficients. A balance between computational costs and the attainment of accurate results suggested the use of a first-order forward scheme to approximate time derivatives and a second order scheme to approximate spatial derivatives (Roache 1972). A further variable $\tilde{\eta}$ has been defined,

$$\tilde{\eta} = \ln \frac{\eta + b}{b} \tag{19}$$

and a constant spatial step $\Delta\tilde{\eta}$ along the $\tilde{\eta}$-direction has been used. The variable $\tilde{\eta}$ has been introduced in order to stretch the region near the bottom where the gradients of the dependent variables are larger. In (19) b is a constant, the value of which has been appropriately chosen (see table 1).

With these approximations, Ω_n inside the computational domain at a new time level is determined explicitly starting from the knowledge of Ω_n and Ψ_n at the previous time level. Such updated values of Ω_n allow the solution of (17) for Ψ_n to be obtained at the new time level with the following boundary conditions:

$$\frac{\partial \Psi_n}{\partial \eta} = \begin{cases} \sin(t) & \text{for} \quad n = 0 \\ 0 & \text{for} \quad n \neq 0 \end{cases} \quad \text{for} \quad \eta = \eta_{\mathrm{fin}}, \tag{20a}$$

$$\Psi_n = 0 \quad \text{at} \quad \eta = 0, \tag{20b}$$

where η_{fin} has been chosen equal to $\frac{2}{3}$ the dimensionless wavelength l of the ripple.

Run	h	l	R_δ	η_{fin}	b	N	M	t_{fin}	Δt
1	6.7	33.3	50	22.22	90.37	128	128	10π	5.0×10^{-4}
2	5.0	33.3	50	22.22	90.37	128	128	10π	—
3	2.3	33.3	50	22.22	90.37	128	128	8π	—
4	1.7	33.3	50	22.22	6.63	64	64	8π	—
5	2.5	16.7	25	11.11	19.20	64	64	4π	—
6	7.5	50.0	75	33.33	18.76	128	128	4π	—
7	2.5	16.7	50	11.11	19.20	64	64	8π	—
8	3.0	20.0	50	13.33	16.83	64	64	4π	—
9	2.8	25.0	50	16.67	9.78	128	64	6π	—
10	7.5	50.0	50	33.33	18.76	128	128	6π	—
11	1.9	12.5	50	11.11	19.20	64	64	4π	—
12	1.5	10.0	50	11.11	19.20	64	64	4π	—
13	5.0	33.3	100	22.22	90.37	128	128	4π	1.5×10^{-4}
14	7.5	50.0	100	33.33	18.76	128	128	4π	—
15	10.0	66.7	100	44.45	13.61	128	128	4π	—
16	10.0	66.7	150	44.45	13.61	128	128	4π	—
17	3.07	12.27	48.75	11.11	19.20	64	64	6π	5.0×10^{-4}
18	0.04	17.95	0.1	18.0	8.45	4	64	30π	—
19	0.05	114.2	40	114.0	6.51	4	128	30π	—
20	0.04	41.88	0.1	42.0	14.0	4	128	30π	—
21	4.71	148.2	14.14	148.0	5.76	16	128	30π	—
22	14.1	148.2	14.14	148.0	5.76	32	128	30π	—
23	23.6	148.2	14.14	148.0	5.76	32	128	30π	—
2a	5.0	33.3	50	22.22	90.37	256	256	2π	1.25×10^{-4}
7a	2.5	16.7	50	11.11	19.20	128	128	2π	1.25×10^{-4}
13a	5.0	33.3	100	22.22	90.37	256	256	2π	3.75×10^{-5}

TABLE 1. Physical parameters and characteristics of the numerical grid.

N	M	CPU time per time step (s)
16	64	2.6×10^{-2}
32	64	4.7×10^{-2}
64	64	9.8×10^{-2}
128	64	19.8×10^{-2}
64	16	2.4×10^{-2}
64	32	4.8×10^{-2}
64	128	19.6×10^{-2}

TABLE 2. CPU time per time step

Preliminary computations performed with larger values of η_{fin} show that this choice does not affect the results.

Equations (17) leads to a tridiagonal system for the values assumed by Ψ_n on a regular grid along the $\tilde{\eta}$-direction. The latter system can be solved by standard methods. The last step in the computational cycle consists of the calculation of the new values of Ω_n on the boundaries of the domain. The latter step is accomplished by forcing a vanishing value of Ω_n at η equal to η_{fin} and computing Ω_n at $\eta = 0$ according to the first-order scheme suggested by Thom (1928) and discussed by Roache (1972).

In table 1 the physical parameters considered in the paper are shown along with the number of grid points in the ξ- and η-directions denoted by N and M respectively,

the time step Δt and the constant b employed for the numerical integration. The value of b has been fixed in order to allocate a sufficient number of grid points in the bottom boundary layer.

All the computations have been carried out using the minisuper computer FPS-M64/60 (peak velocity 38 MFLOPS). In table 2 the CPU time required for a time step is shown for different values of N and M.

4. The initial flow field

In order to test the numerical procedure described in the previous section and in particular the numerical scheme suggested by Thom (1928) to generate vorticity along the ripple profile, in this section we compare the numerical results with the results obtained by an asymptotic analysis which holds at the initial stage of the motion. Further tests on the accuracy of the numerical approach will be described in the following section.

The method of the inner and outer expansions is used to solve the problem formulated in §3 for a short time after the start of the motion, even though here we assume that the velocity far from the wall for t larger than zero does not behave like $\sin t$ but rather like $\cos t$. This assumption simplifies the analysis and provides in any case a test for the numerical procedure.

Since the flow is analysed for short time and some of the quantities introduced previously (namely δ^*, T^*) lose their importance, it is useful to introduce new dimensionless variables

$$\left.\begin{aligned} t' = t\frac{U_0^* T^*}{2\pi l^*}, \quad (\xi', \eta') = (\xi, \eta)\frac{\delta^*}{l^*}, \quad h' = h\frac{\delta^*}{l^*}, \\ \psi' = \psi\frac{\delta^*}{l^*}, \quad \omega' = \omega\frac{l^*}{\delta^*}. \end{aligned}\right\} \tag{18}$$

Let us denote by ϵ a small time interval ($\epsilon \ll 1$) and assume that the Reynolds number Re, defined as $Re = U_0^* l^*/\nu$, is large enough for the quantity $\alpha = (\epsilon Re)^{-1}$ to be of order one.

Introducing a time variable τ defined as t'/ϵ, equations (9), (10) and boundary conditions (11), (12) become

$$\frac{\partial \omega'}{\partial \tau} + \frac{\epsilon}{J}\left[\frac{\partial \psi'}{\partial \eta'}\frac{\partial \omega'}{\partial \xi'} - \frac{\partial \psi'}{\partial \xi'}\frac{\partial \omega'}{\partial \eta'}\right] = \frac{\epsilon^2 \alpha}{J}\left[\frac{\partial^2 \omega'}{\partial \xi'^2} + \frac{\partial^2 \omega'}{\partial \eta'^2}\right], \tag{19}$$

$$\frac{\partial^2 \psi'}{\partial \xi'^2} + \frac{\partial^2 \psi'}{\partial \eta'^2} = -J\omega', \tag{20}$$

$$\frac{\partial \psi'}{\partial \xi'} = \frac{\partial \psi'}{\partial \eta'} = 0 \quad \text{at} \quad \eta' = 0, \tag{21}$$

$$\frac{\partial \psi'}{\partial \xi'} \to 0, \quad \frac{\partial \psi'}{\partial \eta'} \to \cos\left(\frac{2\pi l^*}{U_0^* T^*} t'\right) \quad \text{for} \quad \eta' \to \infty. \tag{22}$$

Stream function and vorticity are expanded in a power series of ϵ:

$$\psi' = \psi_0^0 + \epsilon\psi_1^0 + O(\epsilon^2), \tag{23}$$

$$\omega' = \omega_0^0 + \epsilon\omega_1^0 + O(\epsilon^2). \tag{24}$$

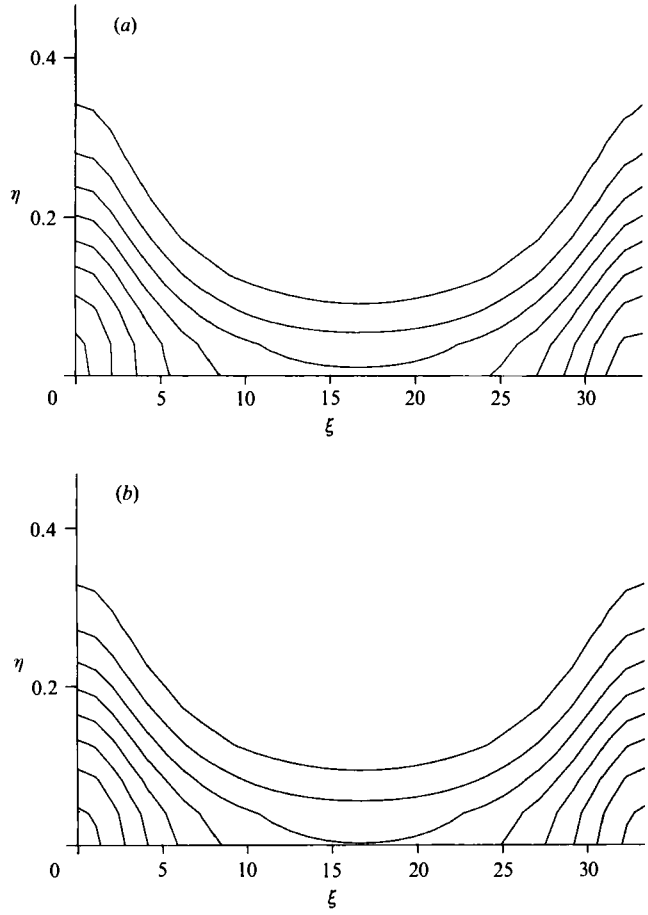

FIGURE 1. Vorticity contours at $t = 0.08$ for $h = 5.0$, $l = 33.33$ and $R_\delta = 50$. (*a*) Numerical results, (*b*) asymptotic results.

Substituting (23), (24) into (19), (22) and making use of the initial condition of irrotationality, it is easy to see that the flow is irrotational to all orders in ϵ. It follows that

$$\omega_0^0 = 0: \quad \psi_0^0 = B_0(\tau)\,\eta' + \sum_{n=-\infty}^{+\infty} A_{n0}(\tau)\,\mathrm{e}^{-2\pi n\eta'}\,\mathrm{e}^{\mathrm{i}2\pi n\xi'}, \tag{25}$$

$$\omega_1^0 = 0: \quad \psi_1^0 = B_1(\tau)\,\eta' + \sum_{n=-\infty}^{+\infty} A_{n1}(\tau)\,\mathrm{e}^{-2\pi n\eta'}\,\mathrm{e}^{\mathrm{i}2\pi n\xi'}. \tag{26}$$

Boundary condition (22) gives $B_0(\tau) = 1$, $B_1(\tau) = 0$ and suggests that A_{n0} and A_{n1} vanish for $n < 0$. Since we cannot force (21), the existence of a region of non-uniformity near the ripple profile is inferred with thickness of order ϵ.

Let us stretch this region by introducing an inner variable Y such that

$$Y = \eta'/\epsilon. \tag{27}$$

Stream function and vorticity are rescaled in the inner layer as follows:

$$\psi^i = e[\psi_0^i + \epsilon\psi_1^i + O(\epsilon^2)], \tag{28}$$

$$\omega^i = \frac{1}{e}[w_0^i + \epsilon\omega_1^i + O(\epsilon^2)]. \tag{29}$$

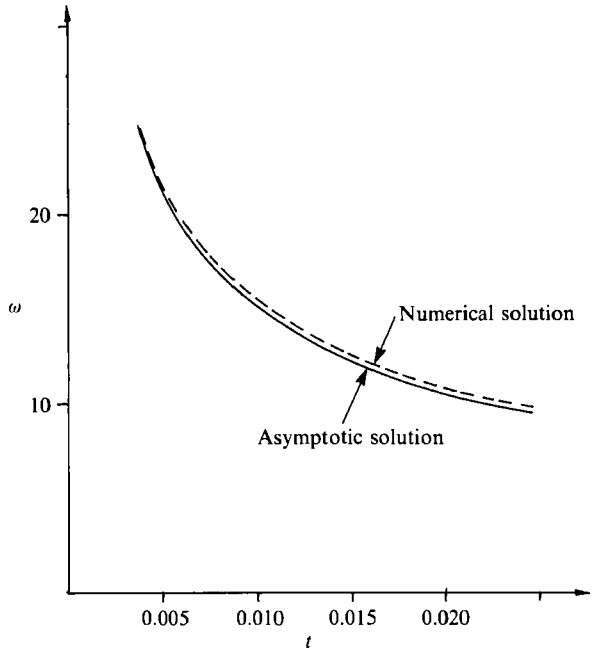

FIGURE 2. Vorticity time development at the ripple crest ($R_\delta = 50$, $h = 5.0$, $l = 33.33$).

Substituting (27), (29) into (19) and (22) and equating like powers of ϵ, at the leading order we find a problem which is identical to that obtained for the impulsively started flow past a plane surface (the Rayleigh problem), except that the local first-order outer velocity on the ripple profile should be used instead of the constant impulse velocity. The solution is then

$$\psi_0^i = C_0(\xi')\left\{Y\,\mathrm{erf}\left[\frac{Y}{2(\alpha\tau/J_0(\xi'))^{\frac{1}{2}}}\right]-2\left[\frac{\alpha\tau}{\pi J_0(\xi')}\left(1-\exp\left[-\frac{Y^2J_0(\xi')}{4\alpha\tau}\right]\right)\right]^{\frac{1}{2}}\right\}+D_0(\xi')\,Y, \tag{30}$$

$$\omega_0^i = -C_0(\xi')\frac{1}{[\pi\alpha\tau J_0(\xi')]^{\frac{1}{2}}}\exp\left(-\frac{Y^2J_0(\xi')}{4\alpha\tau}\right), \tag{31}$$

where $J_0(\xi')$ is the leading-order term of the expansion of $J(\xi',\eta')$ near the ripple profile:

$$J_0(\xi') = 1+(\pi h')^2-2h'\pi\cos 2\pi\xi'. \tag{32}$$

Applying the boundary conditions at the ripple profile and the asymptotic matching principle (Van Dyke 1975), the constants C_0, D_0, A_{n0} can be easily obtained.

Higher-order components of the inner solution are not determined as the present solution is mainly aimed at providing an independent check for the numerical algorithm.

Having an outer expansion valid in the outer region and an inner expansion valid in the inner region, we can form a single composite expansion which is uniformly valid throughout the whole flow field (Van Dyke 1975).

A comparison between the vorticity field obtained by the procedure just described and that obtained by the numerical approach is shown in figure 1 for particular values of the parameters. The qualitative and quantitative agreement is satisfactory

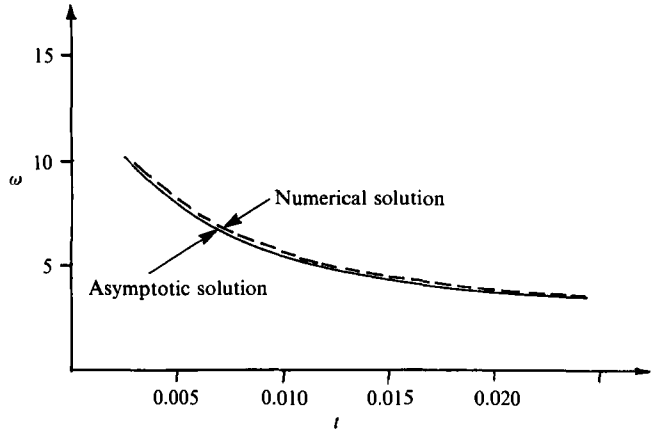

FIGURE 3. Vorticity time development at the ripple trough ($R_\delta = 50$, $h = 5.0$, $l = 33.33$).

and supports the validity of the numerical approach, even though in the numerical calculations the vorticity field is not symmetric because of convective effects which are ignored at the leading order in the asymptotic analysis. The values attained by the vorticity respectively at the ripple crest and trough as functions of time are shown in figures 2 and 3, which include both the asymptotic and the numerical results. The discrepancy due both to the approximations introduced in the numerical approach and to the terms ignored in the asymptotic analysis appears to be quite small. Hence it is possible to conclude that the agreement between the two solutions for small times is good, which suggests the suitability of the numerical scheme employed (Thom 1928) to generate vorticity at the solid boundary. Results similar to those reported in figures 1–3 can be obtained for different values of the parameters.

5. Discussion of results

Before discussing the case of ripples of finite amplitude it is instructive to consider ripples of infinitesimal amplitude.

For bottom waviness characterized by a vanishing amplitude it is possible to linearize the problem discussed in §2 and obtain a solution in analytical form. The latter is presented in a paper by Lyne (1971) for values of kR_δ much smaller or much larger than one and in Vittori (1989), Hara & Mei (1990), Blondeaux (1990) for kR_δ of order one. Vittori (1989) and Blondeaux (1990) assumed the amplitude of the bottom waviness to be much smaller than δ^* while Hara & Mei (1990) developed their analysis assuming small values of the ripple steepness h/l.

The above analytical solutions show the flow to consist of two contributions: one periodic in time and the other time independent. The steady part consists of recirculating cells whose form, intensity and direction depend on the values of k and R_δ. A discussion of the flow field pattern for ripples of infinitesimal amplitude is outside the scope of the present paper; the interested reader is referred to the papers mentioned above. However, the numerical solution described in §3 has been checked for small values of h against the analytical solutions in order to further ascertain the accuracy of the numerical approach.

In figure 4 (*a–c*) the contours of the steady part of the stream function obtained by

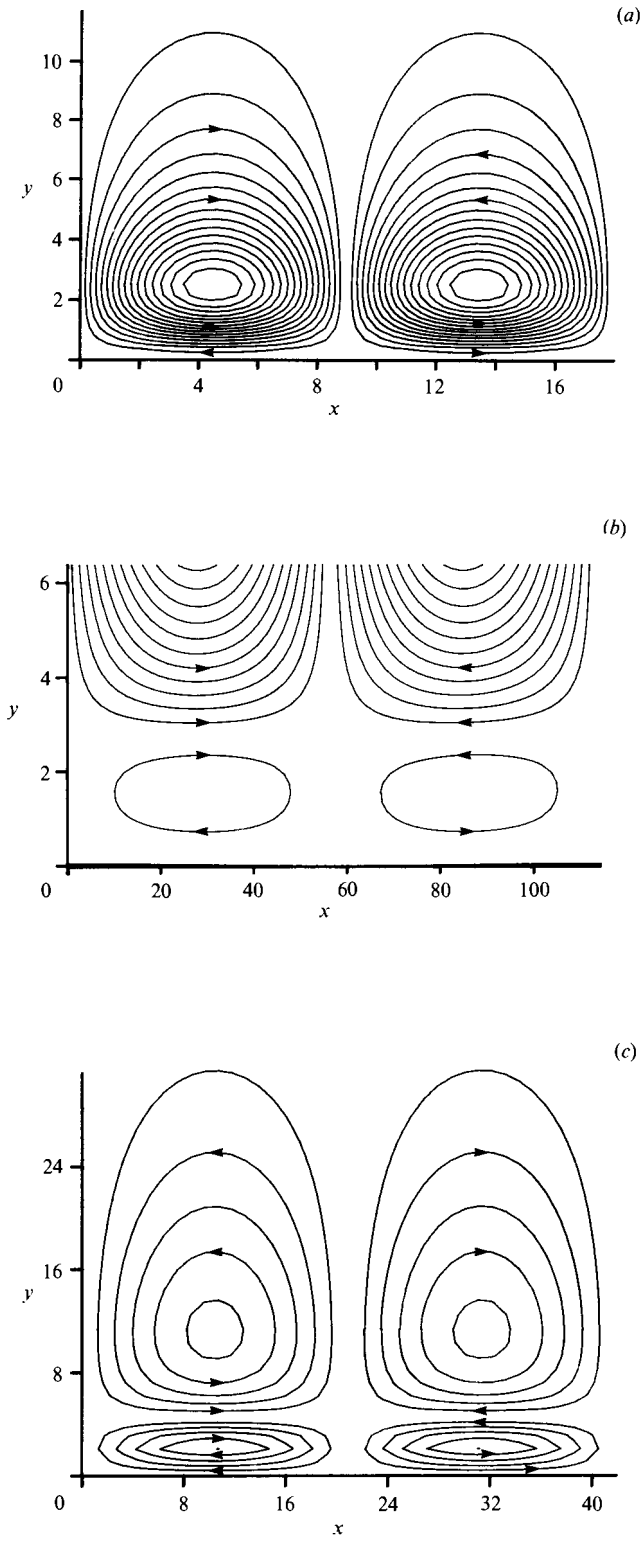

FIGURE 4(*a–c*). For caption see facing page.

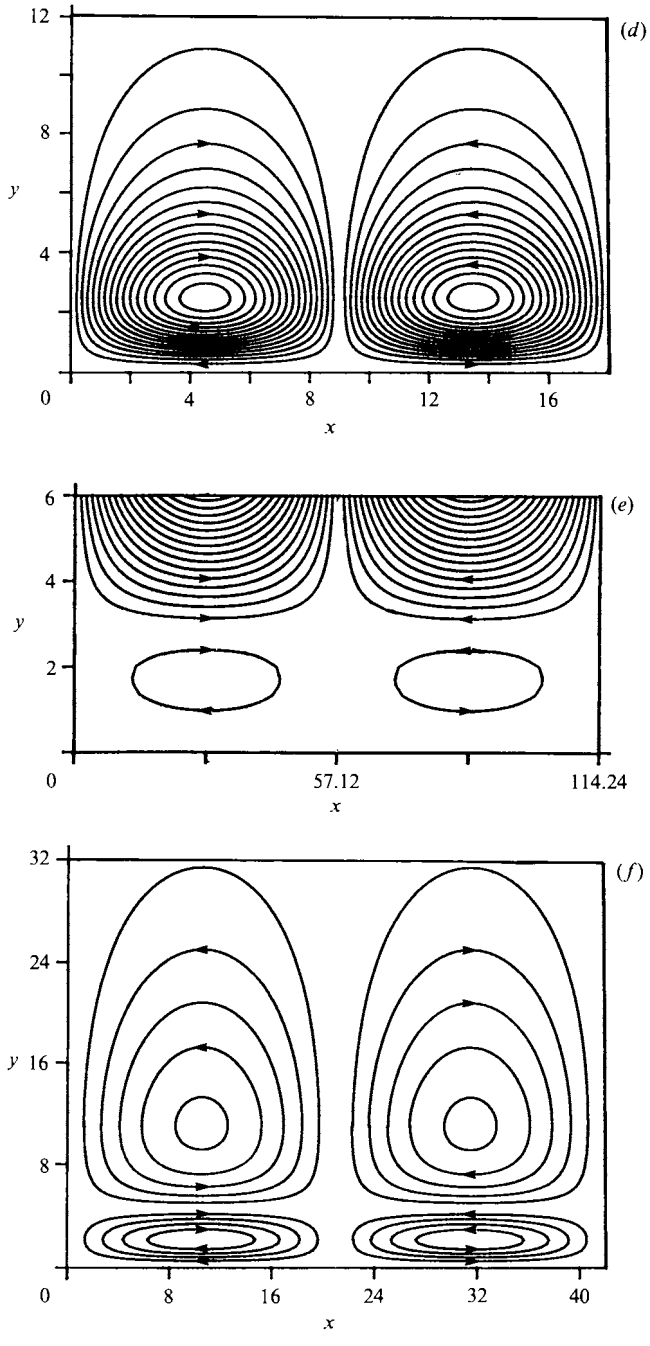

FIGURE 4. Contours of the steady part of the stream function in the oscillatory flow over a wavy wall: (*a*) present results $h = 0.04$, $k = 0.35$, $R_\delta = 0.1$, $\Delta\psi = 2.80 \times 10^{-6}$, (*b*) present results $h = 0.05$, $k = 0.055$, $R_\delta = 40$, $\Delta\psi = 1.37 \times 10^{-4}$, (*c*) present results $h = 0.04$, $k = 0.15$, $R_\delta = 0.1$, $\Delta\psi = 1.56 \times 10^{-6}$, (*d*) Vittori's (1989) results $h = 0.04$, $k = 0.35$, $R_\delta = 0.1$, $\Delta\psi = 2.80 \times 10^{-6}$, (*e*) Hara & Mei's (1990) results $h = 0.05$, $k = 0.055$, $R_\delta = 40$, $\Delta\psi = 1.37 \times 10^{-4}$, (*f*) Blondeaux's (1990) results $h = 0.04$, $k = 0.15$, $R_\delta = 0.1$, $\Delta\psi = 1.56 \times 10^{-6}$.

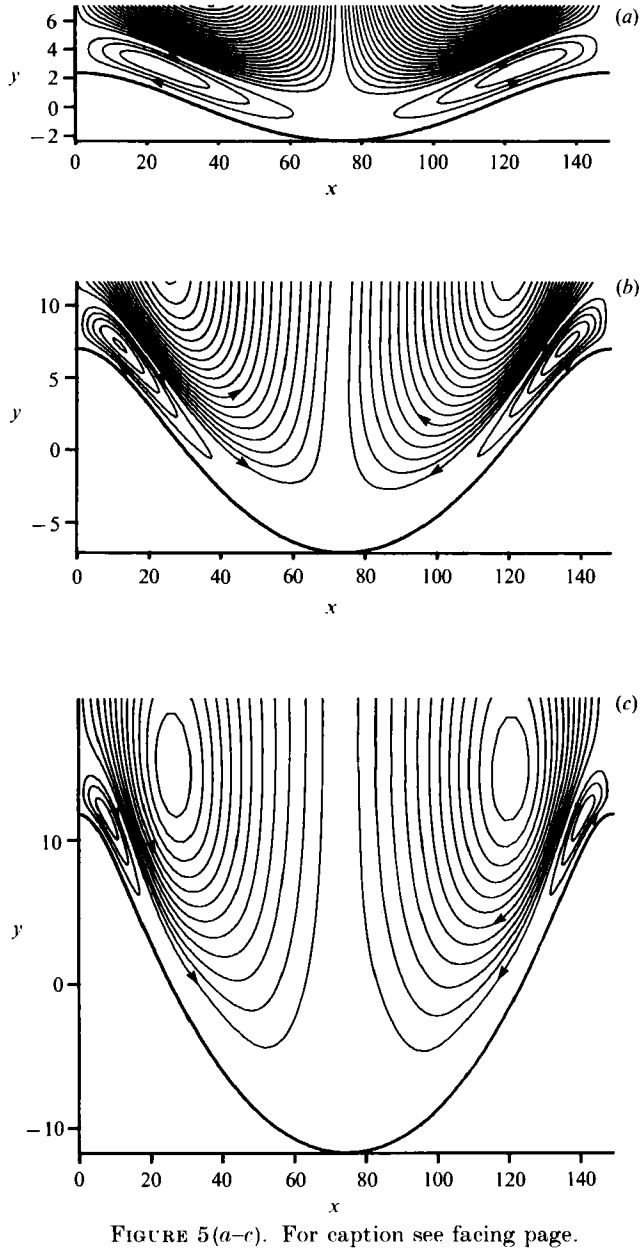

FIGURE 5(*a–c*). For caption see facing page.

means of the present approach are shown for values of the parameters which allow a comparison with some of the results described in Vittori (1989), Hara & Mei (1990) and Blondeaux (1990) and shown herein respectively in figure 4(*d–f*). Taking into account that the contours of the numerical and analytical results are drawn for the same values of the time-average stream function, it can be seen that the qualitative and quantitative agreement is good.

However, it is worth pointing out that, considering larger values of kR_δ, the results by Hara & Mei (1990) deviate from the present results, while the latter still agree satisfactorily with those obtained on the basis of the independent analyses by Vittori

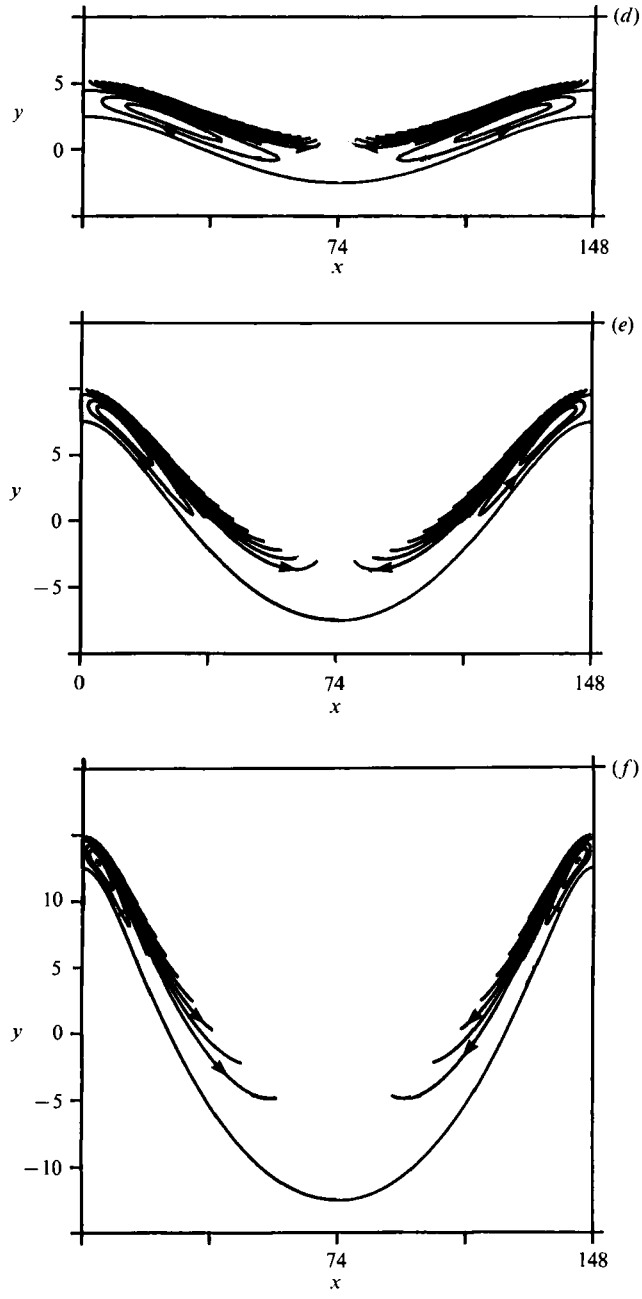

FIGURE 5. Contours of the steady part of the stream function in the oscillatory flow over a wavy wall. Present results: $k = 0.0424$, $R_\delta = 14.14$; (*a*) $h = 4.71$, $\Delta\psi = 0.0018$, (*b*) $h = 14.14$, $\Delta\psi = 0.009$, (*c*) $h = 23.57$, $\Delta\psi = 0.045$. Hara & Mei's (1990) results: $k = 0.0424$, $R_\delta = 14.14$; (*d*) $h = 4.71$, $\Delta\psi = 0.0018$, (*e*) $h = 14.14$, $\Delta\psi = 0.009$, (*f*) $h = 23.57$, $\Delta\psi = 0.045$.

(1989) and Blondeaux (1990). For example for $h = 0.05$, $k = 0.135$ and $R_\delta = 40$ the present results, in accordance with Vittori (1989) and Blondeaux's (1990) findings, show that the maximum value of the steady part of the stream function is located at a distance of approximately $4\delta^*$ from the wall while the results by Hara & Mei

(1990) (see figure 6*b* of their paper) show that the maximum is located at a distance from the wall larger than $12\delta^*$.

Let us now consider ripples of finite amplitude. Even though ripples under field conditions are usually characterized by a wavelength l^* of the same order of magnitude as the amplitude of fluid displacement $U_0^* T^*/2\pi$, let us start by considering small values of the ratio $U_0^* T^*/2\pi l^* = kR_\delta/4\pi$. In this limiting case, i.e. for vanishing values of $kR_\delta/4\pi$, Hara & Mei (1990) showed that an analytical solution of the problem formulated in §2 can be found by means of perturbation methods and it is thus possible to further ascertain the accuracy of the present numerical approach. It should be noted that in order for the asymptotic analysis by Hara & Mei (1990) to be valid R_δ should also be much larger than one.

In figure 5(*a–c*) the contours of the steady part of the stream function obtained by means of the present approach are shown for $k = 0.0424$, $R_\delta = 14.4$ and $h = 4.71$, 14.14, 23.57 respectively. The values of k and h have been fixed in such a way that the present results can be compared with those presented by Hara & Mei (1990) in figure 2(*a–c*) of their paper and shown herein in figure 5(*d–f*). The value of R_δ has been chosen in accordance with a suggestion of Hara & Mei (1990) appearing in the caption to figure 4 of their paper.

The qualitative agreement between the present numerical results and those obtained on the basis of the analytical approach is good. Indeed for $h = 4.71$ both solutions indicate the presence of two thin recirculating cells close to the bottom and two much larger and stronger cells far from it. Moreover, the present results, in accordance with Hara & Mei's (1990) findings, show that the recirculating cells near the bottom decrease in size and become stronger as h increases, while the large recirculating cells far from the bottom tend to move towards the ripple crests and to increase their intensity. However, taking into account that the contours of the numerical and analytical results are drawn for the same values of the time-average stream function, a quantitative discrepancy between the present results and those described by Hara & Mei (1990) can be detected. The discrepancy can be partially explained by observing that the values of the parameters used in Hara & Mei's (1990) paper do not fulfil fully the conditions $k \ll kR_\delta \ll 1$ required for the validity of the analytical approach.

The above comparisons suggest the congruence, the convergence and the accuracy of the numerical scheme, but only in the limiting cases $h \ll 1$ and $k \ll kR_\delta \ll 1$.

In order to get general conclusions it would be necessary to compute each of the cases shown in table 1 with a variety of grid sizes. However, the extent of the parameter space has precluded such numerical experiments and instead only some typical cases have been run using a finer mesh (see table 1). The differences between the solutions computed by different grid sizes have always been found to be smaller than 1% and at this stage such an accuracy has been judged as satisfactory. No plot of the vorticity field is shown for the runs characterized by a finer mesh since it is impossible to distinguish them from the runs characterized by a coarse mesh.

Let us now proceed to discuss the physics of our results. An example of vorticity time development is shown in figure 6 for values of the parameters of physical relevance. The flow starts from rest. It appears that clockwise (assumed positive) vorticity is generated along the bed profile and particularly near the crest of the ripple during the first part of the cycle. Increasing t, the boundary layer thickens on the downstream side of the ripple till flow separates and vorticity of opposite sign is generated at the bottom. Then the rolling up of positive vorticity creates a well-defined vortex structure. The latter induces flow separation on the lee side of the

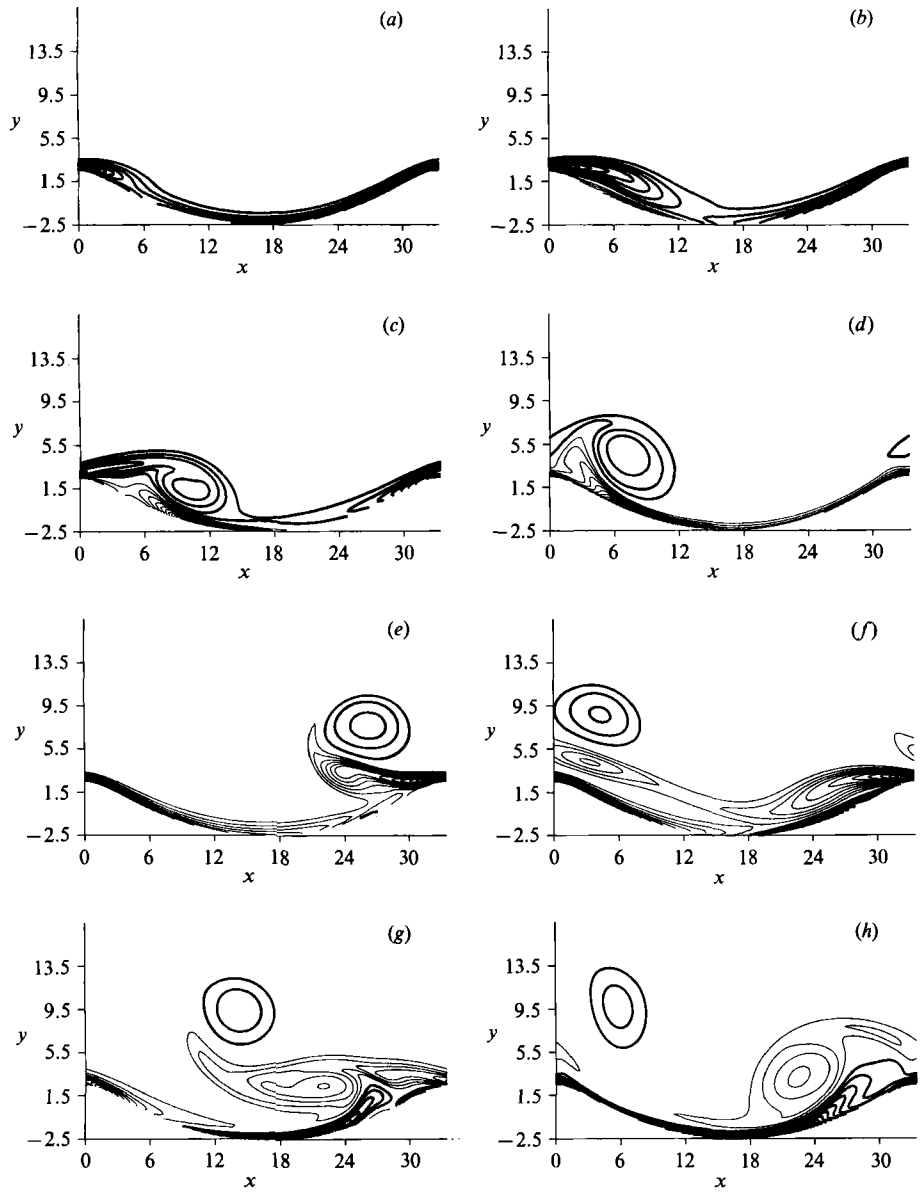

FIGURE 6. Vorticity contours: $\Delta\omega = 0.15$ (——, clockwise vorticity; ——, counterclockwise vorticity), $R_\delta = 50$, $h^*/l^* = 0.15$, $s^*/l^* = 0.75$. (*a*) $t = \frac{1}{4}\pi$; (*b*) $t = \frac{1}{2}\pi$; (*c*) $t = \frac{3}{4}\pi$; (*d*) $t = \pi$; (*e*) $t = \frac{5}{4}\pi$; (*f*) $t = \frac{3}{2}\pi$; (*g*) $t = \frac{7}{4}\pi$; (*h*) $t = 2\pi$.

ripple and the generation of a free shear layer characterized by vorticity of opposite sign. In the second half of the cycle, when the flow reverses, the main vortex structure is no longer reinforced but is simply convected away by the local velocity. The free shear layer originates a new vortex which couples with the previous one, forming a vortex pair which travels along the bed profile moving with its self-induced velocity. Then further counterclockwise vorticity is shed from the ripple crest and when the flow reverses its direction a negative vortex structure is present near the crest and the phenomenon repeats similarly.

The main features of the time development of vorticity have already been described by Longuet-Higgins (1981) by means of a discrete vortex method. Longuet-Higgins (1981) analysed the phenomenon for values of h^*/l^* and s^*/l^* close to ours but assuming an infinite value of R_δ. Longuet-Higgins' (1981) results threw new light on the vorticity dynamics associated with an oscillatory flow over a rippled bed. However, the use of a discrete vortex method unavoidably presents some drawbacks. In fact any approach based on the description of the flow field as a sum of an irrotational component plus a rotational one induced by a finite number of point vortices is unable to detect some important aspects of the phenomenon strictly related to viscous effects. A comparison of the results presented in figure 6 with those described in Longuet-Higgins' (1981) paper shows marked differences:

(i) No significant counterclockwise vorticity is detectable during the first part of the cycle when a discrete vortex method is employed to describe the oscillatory flow over a rippled bed. The present results show that counterclockwise vorticity generated during the first part of the cycle affects the trajectory of the main vortex structure with clockwise circulation. Indeed negative vorticity separates from the ripple profile generating a free shear layer which strongly interacts with positive vorticity (see figure 6*d*). This aspect of the phenomenon is even more evident when larger values of R_δ are considered (see figure 7*b*).

(ii) The vortex pair shed every half-cycle tends to leave the bottom when the vorticity dynamics is computed by a discrete vortex method. The present results on the contrary show that the vortex pair travels close to the bed (see figure 6*f*) and is dissipated near the bed. This difference can be mainly ascribed to the process of vorticity amalgamation usually employed to reduce the large amount of CPU time required by a discrete vortex method. Indeed vorticity amalgamation causes large unnatural velocity.

(iii) The vortex with counterclockwise circulation, which formed a pair with the vortex structures shed during the first half of the cycle, coalesces with the free shear layer of negative vorticity originating from the ripple crest and a unique vortex structure of negative circulation is present near the crest at the end of the first cycle.

(iv) Whenever a vortex structure approaches the bed, the present results show that a free shear layer of opposite vorticity is generated from the wall and the main vortex structure eventually rebounds from the bed, interacting with this free shear layer (see figures 6*g* and 7*d*). This phenomenon cannot be described using a discrete vortex method.

It is worth pointing out that results similar to those described in figure 6 are also obtained for larger values of R_δ as is shown in figure 7 and consequently differences between the present results and those described in Longuet-Higgins (1981) cannot be associated only with the 'small' value of the Reynolds number used in figure 6.

Let us now focus our attention on point (iv). In the oscillatory flow over a rippled bed, regions of concentrated vorticity in an otherwise irrotational flow are present. When one of these vortex structures moves towards the bottom, the boundary layer adjacent to the latter separates and a cell of recirculating flow appears underneath the vortex. This recirculating cell develops very rapidly and leaves the wall when the local thickness of the boundary layer grows dramatically. Then the recirculating cell is ejected into the inviscid region where it is convected away, leaving behind a free shear layer shed from the separation point at the wall. The latter rolls up into a strong eddy which interacts with the primary vortex and causes it to move away from the bottom (see figure 7*d*). When more vortex structures are present, a complex flow field is induced (see figure 15*b*).

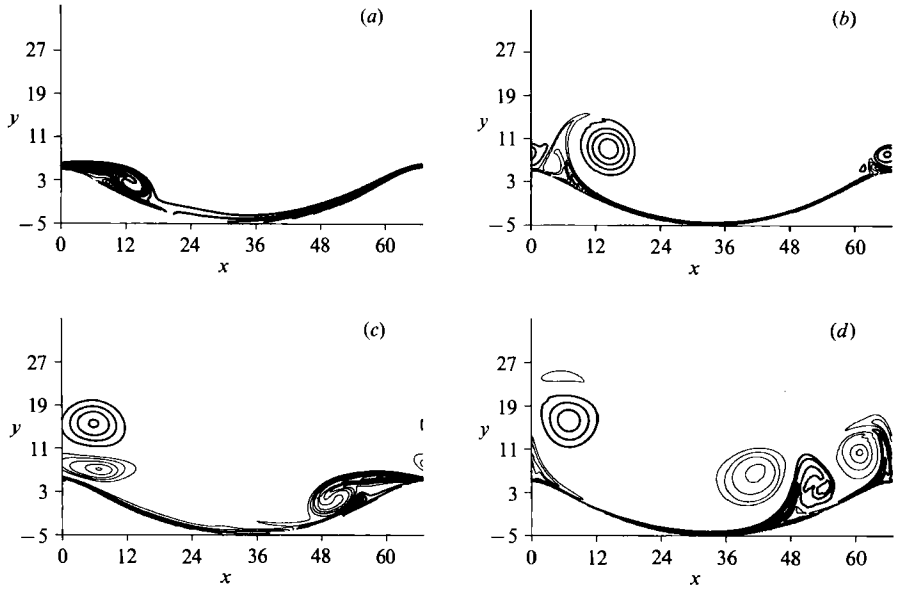

FIGURE 7. Vorticity contours: $\Delta\omega = 0.15$ (——, clockwise vorticity; ——, counterclockwise vorticity), $R_\delta = 100$, $h^*/l^* = 0.15$, $s^*/l^* = 0.75$. (*a*) $t = \frac{1}{2}\pi$; (*b*) $t = \pi$; (*c*) $t = \frac{3}{2}\pi$; (*d*) $t = 2\pi$.

A similar flow pattern can be observed in the interaction between the trailing vortices produced at the tip of an aircraft wing and the boundary layer formed at the ground during take-off or landing. This particular example is important since there is experimental (Harvey & Perry 1971), theoretical (Walker 1978) and numerical (Doligalski & Walker 1984) evidence to show how a vortex structure can induce boundary-layer separation from a flat surface, leading to the formation of a secondary vortex. As pointed out by Doligalski & Walker (1984), separation from a flat wall cannot be handled by means of a discrete vortex method where vortices are periodically introduced into the flow field only at singular geometrical points (Graham 1977) and the no-slip condition for the tangential velocity is not satisfied at solid walls, tacitly assuming that the boundary layers remain thin and passive at all time.

In the phenomenon under consideration a discrete vortex method would predict that an isolated vortex would remain at an almost constant height over a ripple profile, being convected by the local irrotational velocity plus the velocity induced by its image vortex.

Figure 8 shows the streamline pattern during a cycle for the same values of the parameters as in figure 6. Even though some vortex structures can be easily recognized from an inspection of the velocity field (compare figures 6*c*, 6*d*, 6*g* and 6*h* with figures 8*c*, 8*d*, 8*g* and 8*h*), it is almost impossible to recognize some of them (compare figures 6*e* and 6*f* with 8*e* and 8*f*). Since there is experimental evidence that, when the bottom is made of cohesionless material, vortices carry in suspension a lot of sediment, it is clear that an analysis of the velocity field is not sufficient to understand the mechanism through which sediment grains are lifted and maintained in suspension, and the establishment of the vorticity field is necessary.

In the oscillatory flow over a rippled bed, the vorticity time development is controlled by three dimensionless parameters which can be grouped in different ways. In particular the following parameters are significant: (i) the ratio h^*/l^*

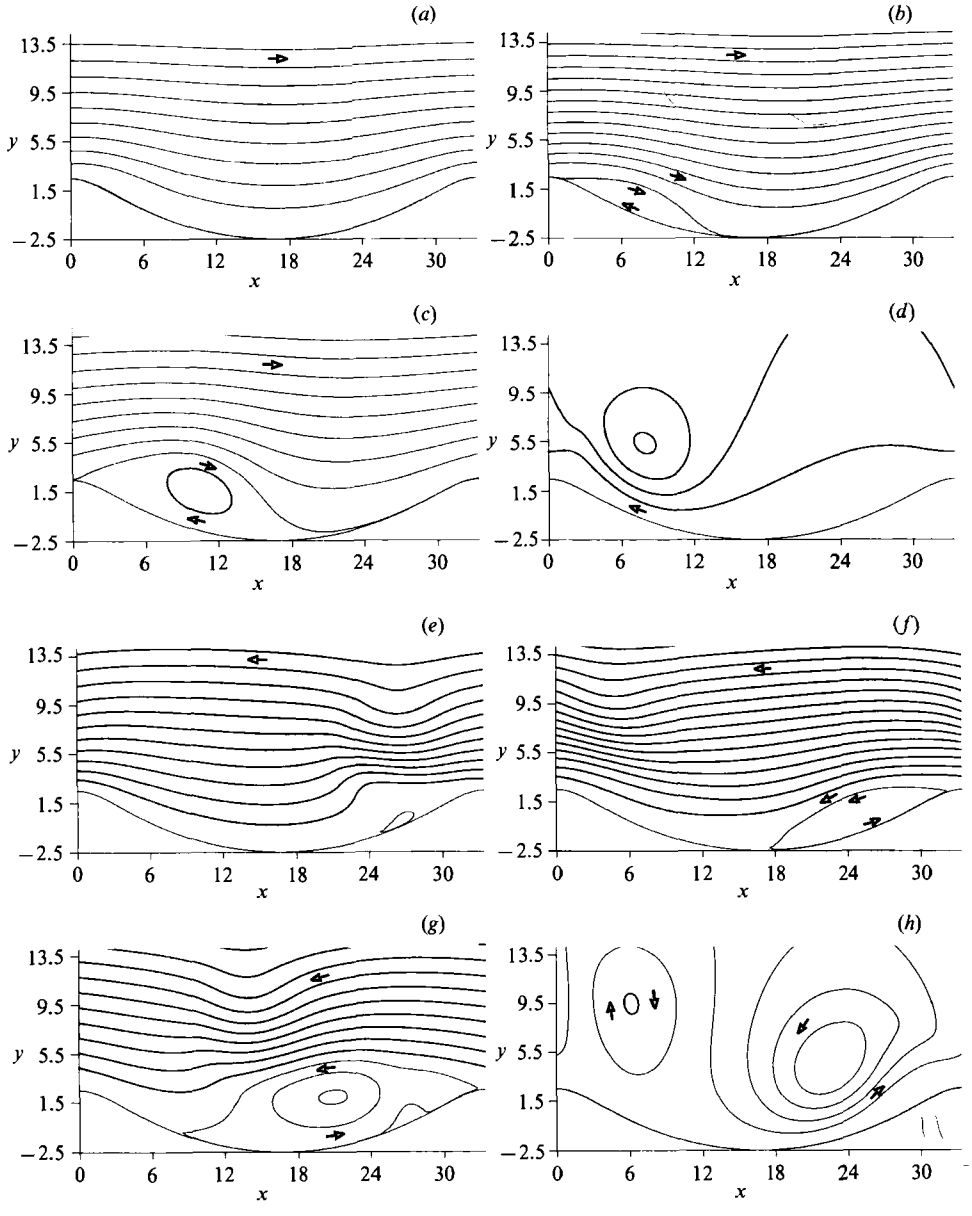

FIGURE 8. Streamline time development ($R_\delta = 50$, $h^*/l^* = 0.15$, $s^*/l^* = 0.75$). (a) $t = \frac{1}{4}\pi$; (b) $t = \frac{1}{2}\pi$; (c) $t = \frac{3}{4}\pi$; (d) $t = \pi$; (e) $t = \frac{5}{4}\pi$; (f) $t = \frac{3}{2}\pi$; (g) $t = \frac{7}{4}\pi$; (h) $t = 2\pi$.

between ripple height and ripple wavelength; (ii) the ratio $U_0^* T^*/2\pi l^*$ between the amplitude of fluid displacement s^* and the ripple wavelength l^*; (iii) the Reynolds number R_δ. It is worth pointing out that using the present notations the ratio s^*/l^* can be written as $kR_\delta/4\pi$.

In the following we will attempt to describe the influence that variations of such parameters exert on the flow field, even though the range of variations of relevant parameters could not be explored fully.

The results presented in figure 6 are for $s^*/l^* = 0.75$, $h^*/l^* = 0.15$ and $R_\delta = 50$ which are possible values for active ripples under field conditions, even though

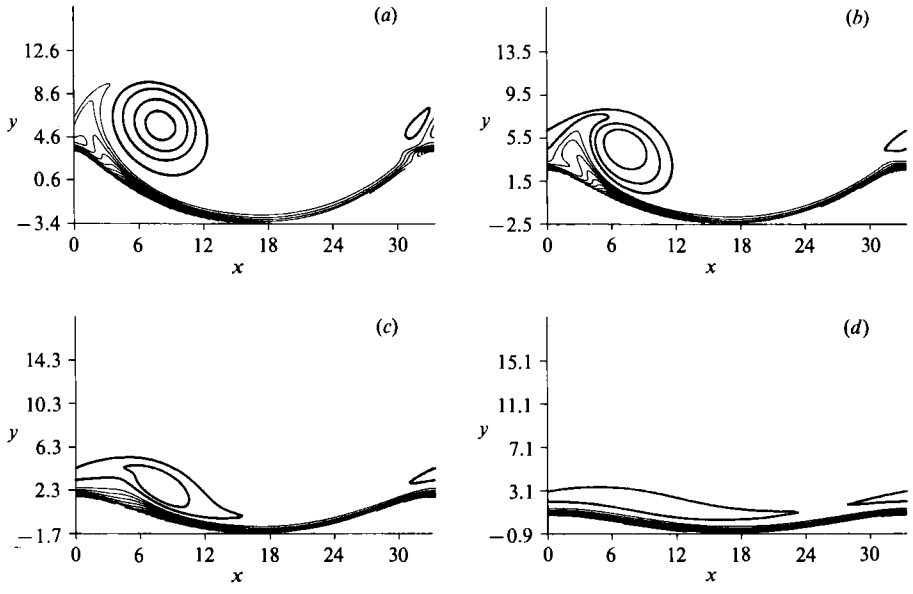

FIGURE 9. Vorticity contours at $t = \pi$: $\Delta\omega = 0.15$ (——, clockwise vorticity; ——, counter-clockwise vorticity) $R_\delta = 50$, $s^*/l^* = 0.75$. (*a*) $h^*/l^* = 0.20$; (*b*) $h^*/l^* = 0.15$; (*c*) $h^*/l^* = 0.10$; (*d*) $h^*/l^* = 0.05$.

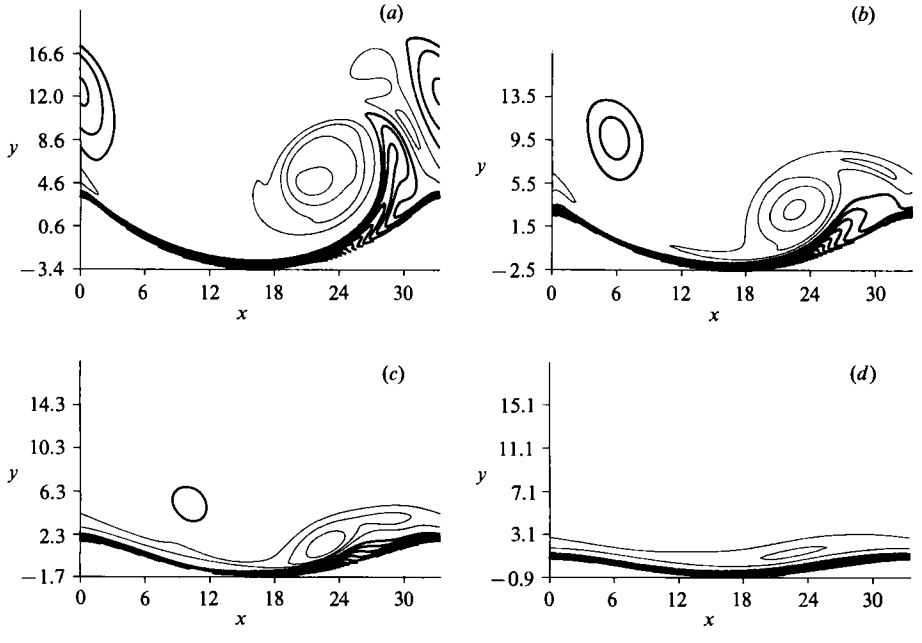

FIGURE 10. Vorticity contours at $t = 2\pi$: $\Delta\omega = 0.15$ (——, clockwise vorticity; ——, counter-clockwise vorticity) $R_\delta = 50$, $s^*/l^* = 0.75$. (*a*) $h^*/l^* = 0.20$; (*b*) $h^*/l^* = 0.15$; (*c*) $h^*/l^* = 0.10$; (*d*) $h^*/l^* = 0.05$.

usually the Reynolds number of the bottom boundary layer takes larger values. Figures 9 and 10 show the vorticity field for the same values of s^*/l^* and R_δ but for different ripple heights. For brevity only two instants of the cycle are shown. On decreasing the value of h^*/l^*, the intensity of the vortex structures shed from the

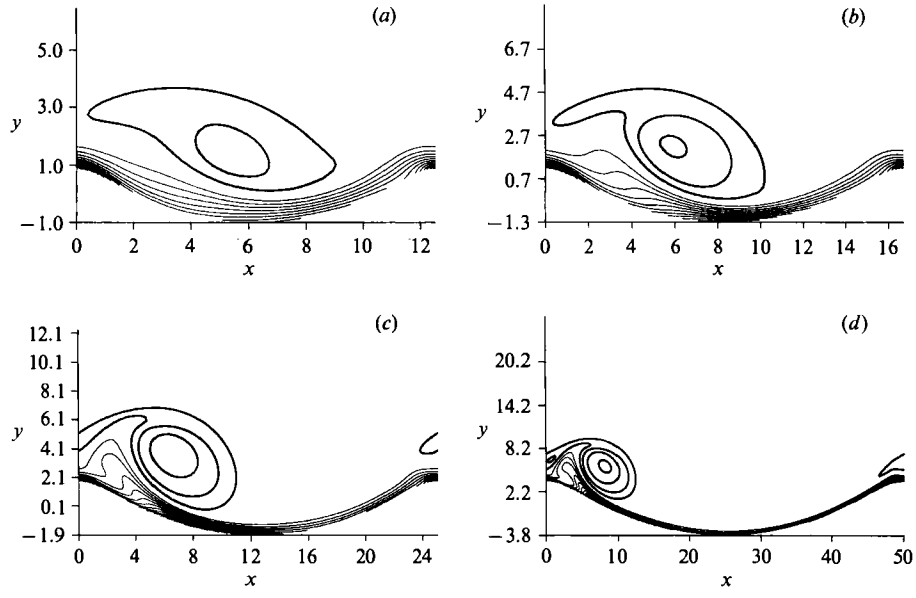

FIGURE 11. Vorticity contours at $t = \pi$: $\Delta\omega = 0.15$ (——, clockwise vorticity; – – –, counter-clockwise vorticity) $R_\delta = 50$, $h^*/l^* = 0.15$. (*a*) $s^*/l^* = 2.0$; (*b*) $s^*/l^* = 1.5$; (*c*) $s^*/l^* = 1.0$; (*d*) $s^*/l^* = 0.5$.

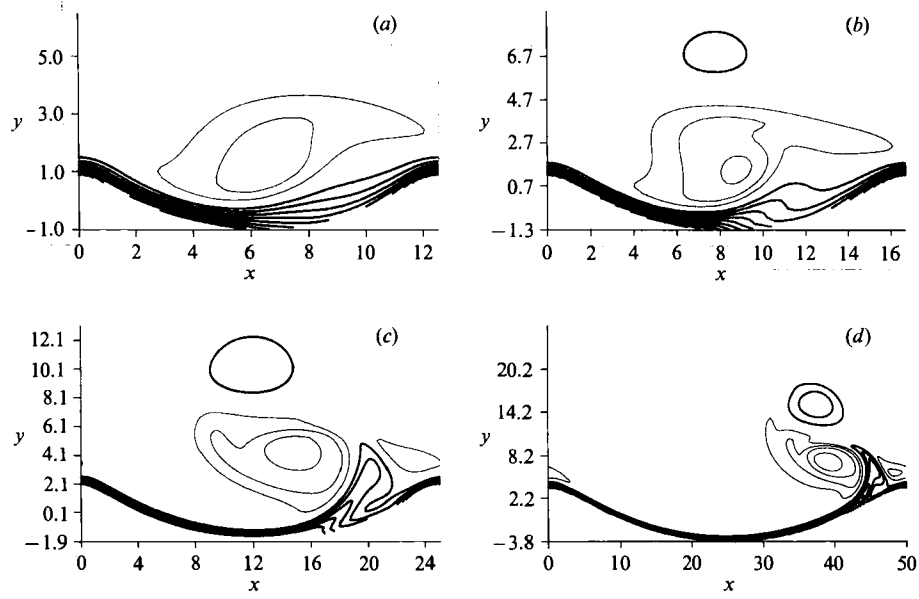

FIGURE 12. Vorticity contours at $t = 2\pi$: $\Delta\omega = 0.15$ (——, clockwise vorticity; – – –, counter-clockwise vorticity) $R_\delta = 50$, $h^*/l^* = 0.15$. (*a*) $s^*/l^* = 2.0$; (*b*) $s^*/l^* = 1.5$; (*c*) $s^*/l^* = 1.0$; (*d*) $s^*/l^* = 0.5$.

ripple crests decreases till only a boundary layer adjacent to the bottom can be recognized. The results shown in figures 9 and 10 seem to support the criterion proposed by Sleath (1984) that the boundary layer adjacent to the bottom separates when h^*/l^* exceeds the 'critical' value 0.1. However it should be pointed out that this behaviour of the vorticity field is present when s^*/l^* is equal to 0.75 and R_δ

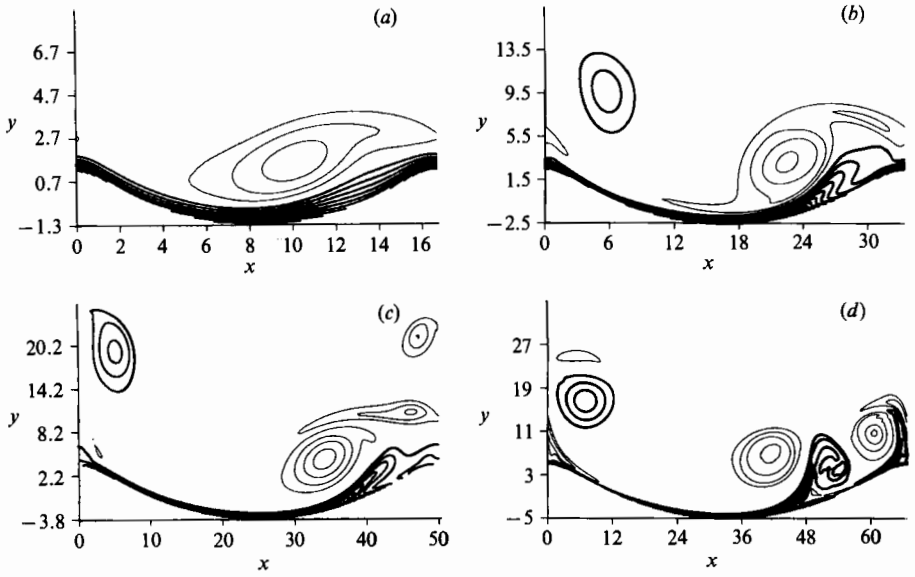

FIGURE 13. Vorticity contours at $t = 2\pi$: $\Delta\omega = 0.15$ (——, clockwise vorticity; ——, counter-clockwise vorticity) $h^*/l^* = 0.15$, $s^*/l^* = 0.75$. (*a*) $R_\delta = 25$; (*b*) $R_\delta = 50$; (*c*) $R_\delta = 75$; (*d*) $R_\delta = 100$.

assumes large values. For example flow separation is absent for h^*/l^* larger than 0.1 when R_δ tends to vanish. Thus Sleath's (1984) criterion is not generally valid but it works for ripples under sea waves which usually are characterized by values of s^*/l^* close to 0.75 and by large values of R_δ.

In figures 11 and 12 the vorticity field is shown for fixed values of h^*/l^* and R_δ but for different values of s^*/l^*. Since the ratio between the amplitude of fluid oscillations and the ripple wavelength is equal to $kR_\delta/4\pi$, an increase of s^*/l^* for fixed values of h^*/l^* and R_δ implies an increase of δ^*/l^* and of δ^*/h^*. It can be concluded that an increase of s^*/l^* causes ripple dimensions to decrease with respect to the viscous characteristic length δ^*. Thus an increase of s^*/l^* implies larger viscous effects and a more rapid spread of vorticity. Indeed in figures 11 and 12 it can be seen that for large values of s^*/l^*, no well-defined vortex structure is detectable near the bed.

When s^*/l^* assumes values larger than those of figures 11 and 12 and tends to infinity, ripples behave like a bed roughness of small height and small length with respect to the boundary-layer thickness δ^*. The flow field differs from Stokes solution only within a region adjacent to the bottom, the thickness of which is of order h^*. These results provide support to the statement that roughness does not affect the velocity field if the flow is laminar.

The same qualitative behaviour can be observed in figure 13 where different values of R_δ are considered with fixed values of h^*/l^* and s^*/l^*. Indeed a decrease of R_δ implies larger viscous effects and less important convective effects.

For ripple wavelength and height as large as δ^*, an attempt can be made to compare the present results with those obtained by Ralph (1986, 1988) and Sobey (1980, 1982, 1983), who studied the oscillatory flow in wavy channels characterized by wavelengths and heights of the wall waviness of the same order of magnitude as the viscous characteristic length. Because of the differences in the geometry studied by the authors mentioned above the comparison can only be qualitative.

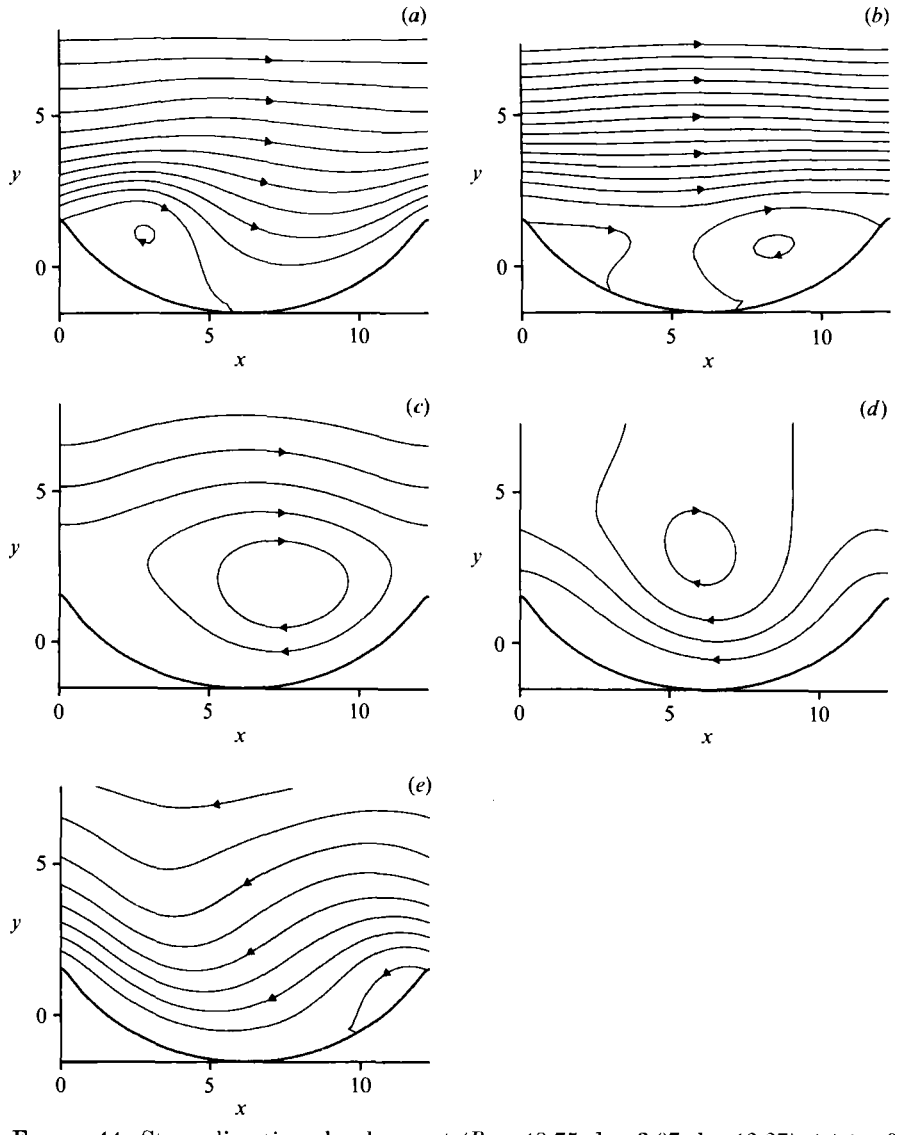

FIGURE 14. Streamline time development ($R_\delta = 48.75$, $h = 3.07$, $l = 12.27$). (a) $t = 0.628$; (b) $t = 1.571$; (c) $t = 2.827$; (d) $t = 3.142$; (e) $t = 3.456$.

In figure 14 the computed instantaneous streamlines of the oscillatory flow over a rippled bed are drawn for $h = 3.07$, $l = 12.3$ and $R_\delta = 48.75$. These values of the parameters allow a qualitative comparison of present results with those presented by Sobey (1982) in figure 1 of his paper. As the external velocity increases, separation occurs at the lee side of the ripple. Subsequent increases in the velocity cause the appearance of another recirculating cell along the ripple profile. As flow decelerates, the recirculating cell grows and fills almost all the ripple trough. Then flow reverses and a new counter-rotating recirculating cell appears, produced by flow separation, thus repeating the process of vortex generation, growth, expansion and decay. Except for expected quantitative differences, the same time development of the flow was found by Sobey (1982).

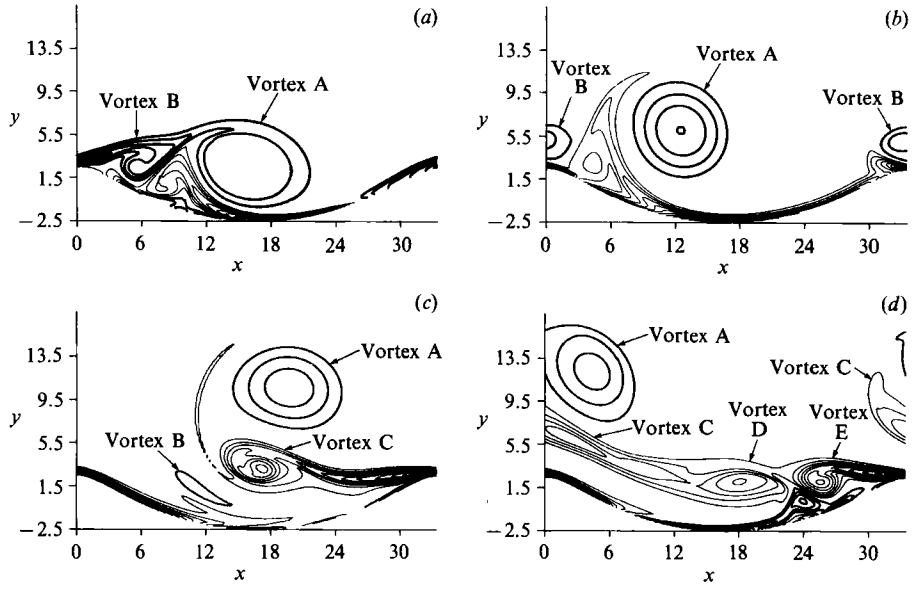

FIGURE 15. Vorticity contours: $\Delta\omega = 0.15$ (——, clockwise vorticity; ——, counterclockwise vorticity) $R_\delta = 100$, $h^*/l^* = 0.15$, $s^*/l^* = 1.5$. (*a*) $t = \frac{3}{4}\pi$; (*b*) $t = \pi$; (*c*) $t = \frac{5}{4}\pi$; (*d*) $t = \frac{3}{2}\pi$.

Similar results have also been found by Ralph (1988) (see figure 3 of his paper) for slightly different values of the parameters. Further comparisons have not been carried out since, as pointed out in the introduction, the present paper is mainly devoted to the study of ripple profiles characterized by a lengthscale much larger than the thickness of the viscous boundary layer at the bottom of sea waves.

Different vorticity fields are obtained for different values of the parameters. As previously pointed out the extent of the parameter space has precluded the computation and description of all the possible cases. In figure 15 the vorticity time development is shown for a part of the cycle when $R_\delta = 100$, $h^*/l^* = 0.15$ and $s^*/l^* = 1.5$. Comparing figure 15(*a*) with figure 6(*c*), which corresponds to the same instant of the cycle but different values of the parameters, it can be seen that for the larger values of R_δ and s^*/l^*, the development of positive vorticity gives rise to two well-defined vortex structures which have an independent time evolution (see figures 15*b* and 15*c*). On the other hand, for the smaller values of R_δ and s^*/l^* only one vortex structure could be recognized.

These findings along with the observation that the vorticity field becomes more complex as time progresses (compare figures 16*a* and 16*b*) seem to preclude a comprehensive presentation of the results. However, the problem is less dramatic when quantities averaged over a wavelength are considered. Indeed the present results can be used to compute quantities of applicative interest such as friction and dissipation factors denoted by f_w and f_e respectively. As previously mentioned, the presence of bottom waviness suggests that the definitions of f_w and f_e should be averaged over a ripple wavelength. Thus we write

$$f_w = \left[\frac{2}{R_\delta l}\int_0^l \left[\left(\int_0^\xi \left(\frac{\partial\omega}{\partial\eta}\right)_{\eta=0} \tfrac{1}{2}hk\sin k\xi\,\mathrm{d}\xi\right) - (1-\tfrac{1}{2}hk\cos\xi)\,\omega\right]\mathrm{d}\xi\right]_{\max}, \tag{33}$$

$$f_e = \left[\frac{3k}{2R_\delta}\int_0^l\int_0^\infty \boldsymbol{JD}:\boldsymbol{D}\,\mathrm{d}\eta\,\mathrm{d}\xi\right], \tag{34}$$

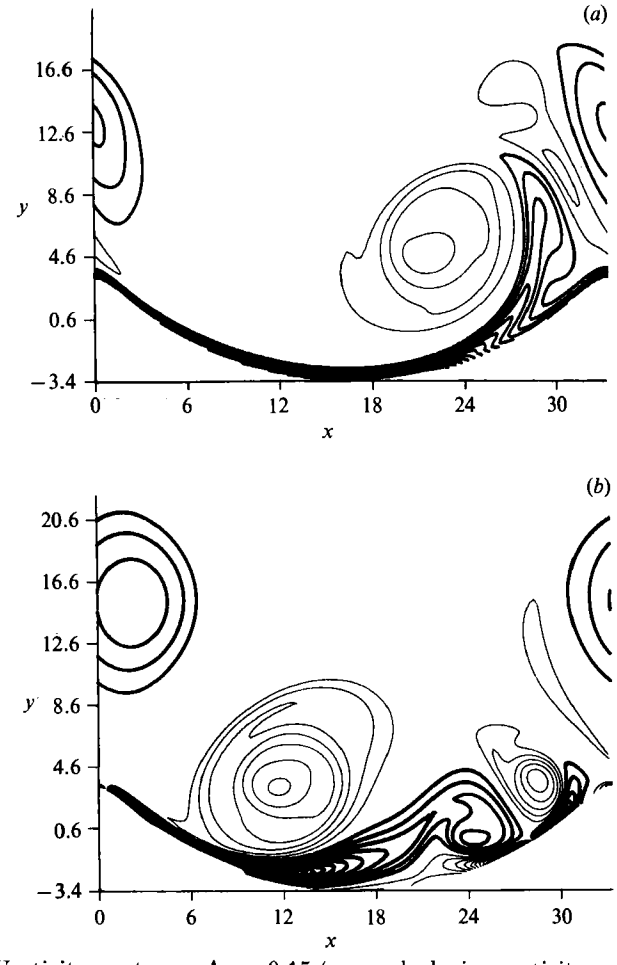

FIGURE 16. Vorticity contours: $\Delta\omega = 0.15$ (——, clockwise vorticity; ——, counterclockwise vorticity) $R_\delta = 50$, $s^*/l^* = 0.75$, $h^*/l^* = 0.20$. (*a*) $t = 2\pi$; (*b*) $t = 4\pi$.

where $\boldsymbol{D}$ is the strain rate tensor and subscript 'max' denotes the maximum value attained by the quantity in square brackets during a cycle.

Figure 17 shows the behaviour of $f_e(t)$ for some typical cases, namely runs 3, 2, 7. In the first case before a transition period the flow becomes periodic and no uncertainty is present in defining the dissipation factor $\bar{f}_e$ averaged over a cycle. In the latter two cases the flow does not reach a time-periodic behaviour even after many cycles. Moreover, results obtained so far seem to suggest that such periodic behaviour will never be attained by the flow. This non-periodic behaviour of a flow driven by a sinusoidal forcing has already been found by other authors in different geometries (see for example Bearman, Graham & Singh 1979). However, a sort of regime configuration is attained in this situation, as can be seen looking at figure 18 where the vorticity contours are plotted after 1, 2, 3, 5 cycles for run 2. Indeed even though the vorticity field is never the same, the main vortex structures detected at the end of the first cycle can always be identified and the qualitative description of the flow based on figure 6 does not change.

Thus, it seems reasonable to assume that knowledge of the structure of the flow field in the first few cycles gives a reliable qualitative picture of vorticity dynamics

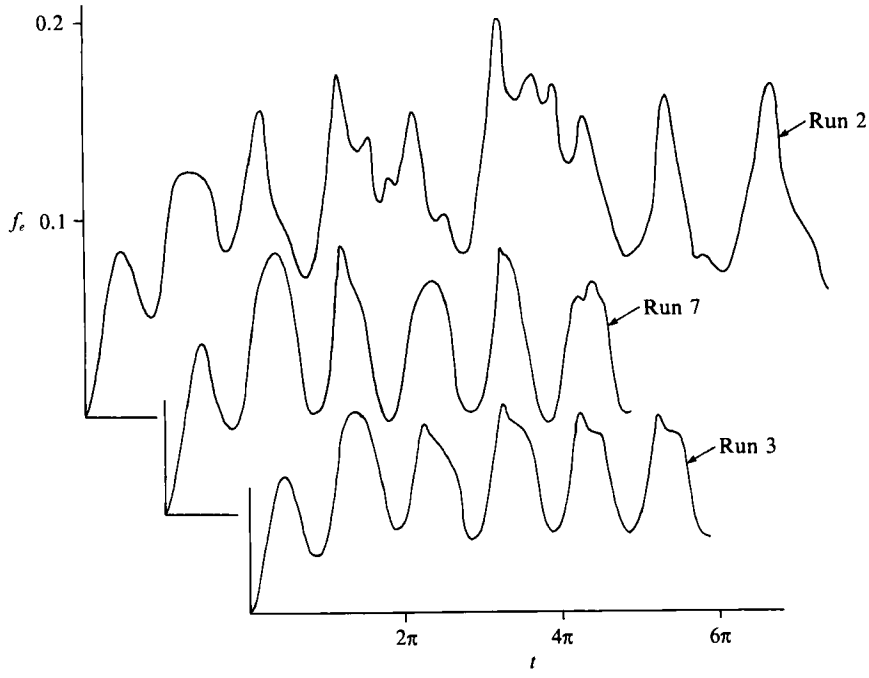

FIGURE 17. Instantaneous dissipation factor $f_e(t)$.

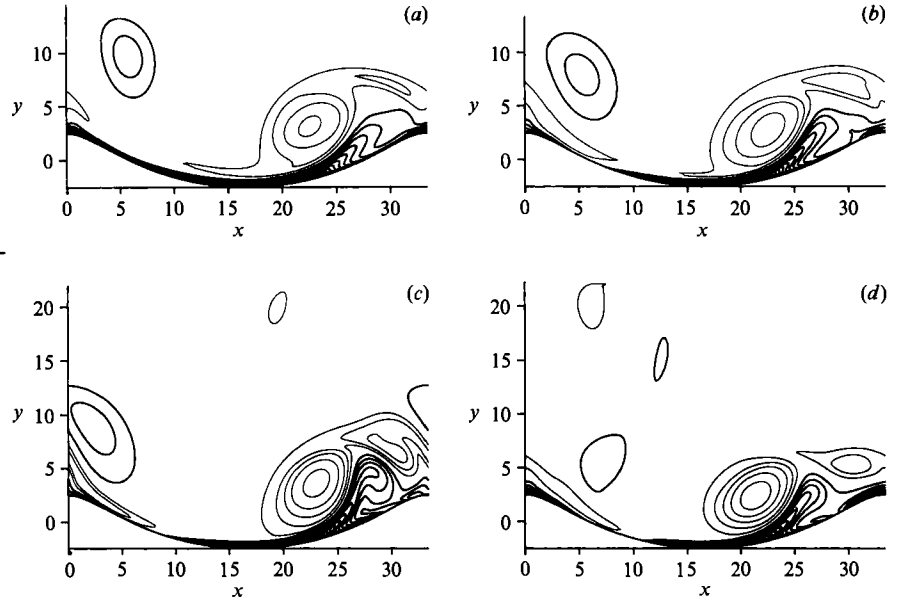

FIGURE 18. Vorticity contours: $\Delta\omega = 0.15$ (——, clockwise vorticity; ——, counterclockwise vorticity) $R_\delta = 50$, $h^*/l^* = 0.15$, $s^*/l^* = 0.75$. (*a*) $t = 2\pi$; (*b*) $t = 4\pi$; (*c*) $t = 6\pi$; (*d*) $t = 10\pi$.

for the whole process. A deeper understanding of a possible underlying attractor in the solution of the time development for the flow field requires further work on single runs carried out for a large number of cycles. Such a study is in progress.

The non-periodic flow behaviour detected in some runs is such that the average

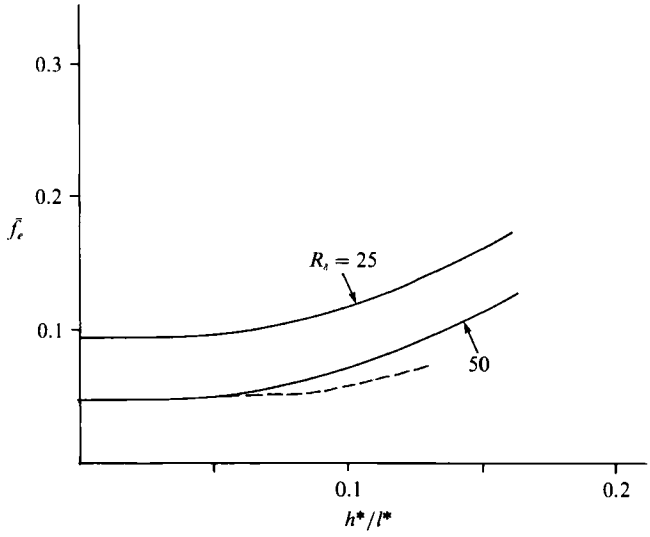

FIGURE 19. Dissipation factor averaged over a cycle plotted versus h^*/l^* for $s^*/l^* = 0.75$ and different values of R_δ (——, present results; – – –, Vittori's (1988) results).

Run number	t (0.2π)	$(2\pi, 4\pi)$	$(4\pi, 6\pi)$	$(6\pi, 8\pi)$	$(8\pi, 10\pi)$	Mean
2	0.082	0.117	0.136	0.110	0.125	0.114
3	0.059	0.071	0.071	0.071	—	—
7	0.075	0.087	0.086	0.087	—	—

TABLE 3. Values of the time-average dissipation factor $\bar{f}_e$ over various ranges of t.

over a cycle of the dissipation factor depends on time (see table 3 where the average of f_e over successive complete cycles is shown for run 2, 3 and 7). As suggested by Longuet-Higgins (1981), who found the same behaviour of $\bar{f}_e$ when studying the oscillatory flow over a rippled bed by means of a discrete vortex method, it is possible to overcome this shortcoming by introducing, for non-periodic flow, a mean value of $\bar{f}_e$ which is shown in the last column of table 3.

In figure 19 the dissipation factor $\bar{f}_e$ is plotted versus the ratio h^*/l^*, for $s^*/l^* = 0.75$ and $R_\delta = 50$ and 25. As previously discussed, when $\bar{f}_e$ depends on time its mean value computed on the basis of the first cycles is considered. In the same plot a dotted line is shown which corresponds to values of $\bar{f}_e$ obtained analytically with an asymptotic analysis which holds for small values of h^*/l^* (Vittori 1988). When h^*/l^* is smaller than 0.1, theoretical and numerical values of $\bar{f}_e$ agree well. For h^*/l^* larger than 0.1, the computed values of $\bar{f}_e$ are larger than those obtained analytically because the former take into account flow separation. It is worth pointing out that the numerical values of $\bar{f}_e$ fall within the range of the experimental results of Carstens, Nielson & Altinbilek (1969) and Lofquist (1980); however, a detailed quantitative comparison between the present results and experimental data has not been performed since experiments are characterized by relatively large values of the Reynolds number such that the flow in the bottom boundary layer is turbulent. In figure 20 $\bar{f}_e$ is plotted versus s^*/l^* for $h^*/l^* = 0.15$ and $R_\delta = 50$. The

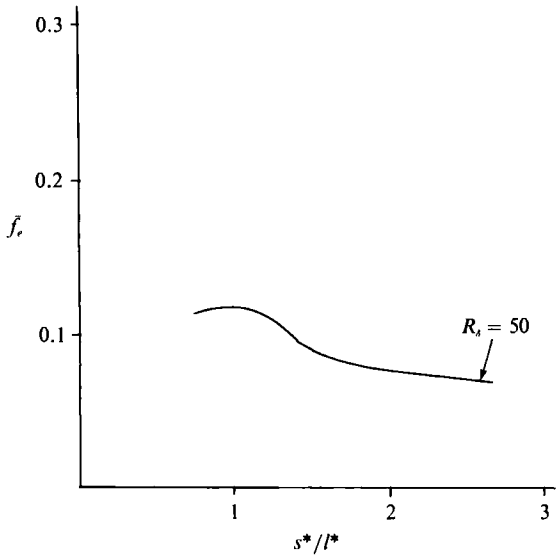

FIGURE 20. Dissipation factor averaged over a cycle plotted versus s^*/l^* for $h^*/l^* = 0.15$ and $R_\delta = 50$.

computer costs have not allowed the computation of $\bar{f}_e$ for different values of the Reynolds number and/or of the ratio h^*/l^*. However, the results obtained so far and shown in figure 20 seem to indicate, according to experimental findings, that the dissipation factor is largest for s^*/l^* approximately equal to 0.75. Incidentally, self-formed ripples are characterized by a wavelength which is generally about two-thirds of the horizontal excursion of the water particles close to the bed, in other words by values of s^*/l^* approximately equal to 0.75.

Similar results are obtained for the friction factor f_w. However, it is more interesting to analyse the spatial distribution of the bed shear stress τ and its time development. Indeed in the present analysis we have considered a fixed bottom profile, but when this assumption is dropped and a cohesionless bottom is considered, the bottom configuration is mainly controlled by the bed shear stress distribution. The spatial and temporal distribution of τ is shown in figure 21 for fixed values of h^*/l^*, s^*/l^* and R_δ. Starting from rest, the bed shear stress is directed according to the outer irrotational flow (positive bed shear stress) and is larger at the ripple crests than at the ripple troughs. For $t = \frac{1}{2}\pi$ a region of bed shear stresses in the direction opposite to that of the outer irrotational flow (negative bed shear stress) appears along the lee side of the ripple. Since this region is related to flow separation and to the generation of negative vorticity along the bed profile, when the latter grows, negative stresses increase their intensity. The appearance of negative vorticity during the first part of the cycle is due to the presence of a large vortex structure of clockwise rotation which induces negative velocity near the bed, even though the outer irrotational flow is positive. When flow reverses and the main vortex structure is no longer strengthened, decaying due to viscous effects, negative bed shear stresses decrease in intensity while positive bed shear stresses appear on the other side of the ripple. Similar results are obtained in the second half of the cycle. Of course this quantitative result changes as different values of the parameters are considered, even though the qualitative behaviour is unaltered if active vortex ripples under field conditions are considered (see for example figure 22). For brevity

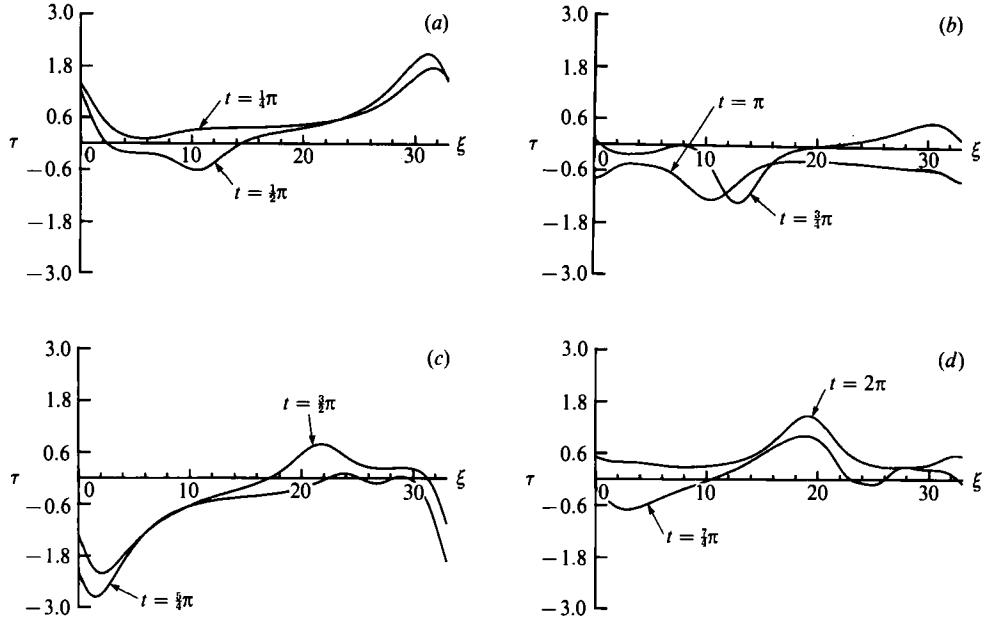

FIGURE 21. Bed shear stress time development. $R_\delta = 50$, $h^*/l^* = 0.15$, $s^*/l^* = 0.75$.

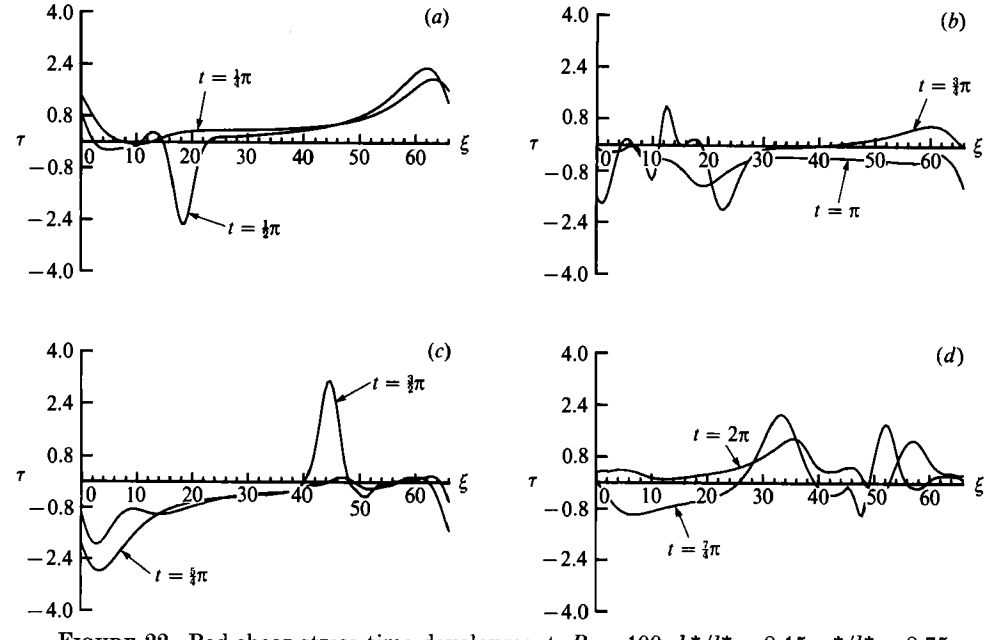

FIGURE 22. Bed shear stress time development. $R_\delta = 100$, $h^*/l^* = 0.15$, $s^*/l^* = 0.75$.

we do not describe in detail the changes on the bed shear stress development produced by variations of the parameters. We only state that the present results could be used in future attempts to study the time development of vortex ripples when the bottom is made of cohesionless material. Hedegaard (1985) tackled the problem mentioned above and in particular focused her attention on small values of the bed shear stress, i.e. when bed load is supposed to give the main contribution to

the total load. However, even for small values of the bed shear stress, the vortex structures generated by flow separation at the ripple crests carry a lot of sediment in suspension. The lack of detailed information on the vorticity field and on the mechanism of sediment transport in suspension forced Hedegaard (1985) to introduce strong approximations. The present results can hopefully be used to study the dynamics of sediment grains in suspension and to gain new information on the suspended load over vortex ripples. Some preliminary work (Blondeaux & Vittori 1990) suggests that starting from knowledge of the vorticity field a qualitative picture of the motion of sediment grains carried in suspension can be obtained. These qualitative results agree with the experimental observations by Nielsen (1979) and Sunamura (1980).

The proposed model is still limited by the assumption of laminar flow. This assumption limits the analysis to values of the Reynolds number R_δ less than a critical value $(R_\delta)_c$. Experimental (Merkly & Thomann 1975; Hino, Sawamoto & Takasu 1976, Tromans 1976) and theoretical (Blondeaux & Seminara 1979) studies seem to indicate that $(R_\delta)_c$ ranges between 100 and 500. Thus even though the present analysis provides results of physical relevance, an extension of the numerical code to the turbulent case is desirable. Turbulence in an oscillatory boundary layer at the bottom of gravity waves can be handled by means of a turbulence model and in this situation Saffman's turbulence model seems particularly suitable as described in Blondeaux (1987). The numerical code can be modified in this respect and no great difficulties are expected.

This work has been partially supported by the Italian Ministry of Education and partially by the National Research Council (CNR) under grant 'Piano finalizzato: Sistemi informatici e calcolo parallelo – Sottoprogetto Calcolo scientifico per grandi sistemi' – No. 8903344.

REFERENCES

AYRTON, H. 1910 The origin and growth of ripple mark. *Proc. R. Soc. Lond.* A **84**, 285–310.

BAR-LEV, M. & YANG, H. T. 1975 Initial flow field over an impulsively started circular cylinder. *J. Fluid Mech.* **72**, 625–647.

BEARMAN, P. W., GRAHAM, J. M. R. & SINGH, S. 1979 Forces on cylinders in harmonically oscillating flow. In *Mechanisms of Wave Induced Forces on Cylinders* (ed. J. H. Shaw). Pitman.

BLONDEAUX, P. 1987 Turbulent boundary layer at the bottom of gravity waves. *J. Hydraul. Res.* **25**, 447–464.

BLONDEAUX, P. 1990 Sand ripples under sea waves. Part 1. Ripple formation. *J. Fluid Mech.* **218**, 1–17.

BLONDEAUX, P. & SEMINARA, G. 1979 Transizione incipiente al fondo di un'onda di gravità. *Att. Acc. Naz. Lincei*, **67**, 408.

BLONDEAUX, P. & VITTORI, G. 1990 Oscillatory flow and sediment motion over a rippled bed. *Proc. XXII Conf. on Coastal Engng, Delft.* ASCE.

CARSTENS, M. R., NIELSON, F. M. & ALTINBILEK, H. D. 1969 Bed forms generated in the laboratory under oscillatory flow. *Tech. Mem.* 28. Coastal Engng Res. Center, Fort Belvoir, VA.

CHRISTIANSEN, J. P. 1973 Vortex methods for flow simulation. *J. Comput. Phys.* **13**, 363.

DOLIGALSKI, T. L. & WALKER, J. D. A. 1984 The boundary layer induced by a convected two-dimensional vortex. *J. Fluid Mech.* **139**, 1–28.

DU TOIT, C. G. & SLEATH, J. F. A. 1981 Velocity measurements close to rippled beds in oscillatory flow. *J. Fluid Mech.* **112**, 71–96.

GRAHAM, J. M. R. 1977 Vortex shedding from sharp edges. *Imperial College Aero. Rep.* 77.06.

HARA, T. & MEI, C. C. 1990 Oscillating flows over periodic ripples. *J. Fluid Mech.* **211**, 183–209.

HARVEY, J. K. & PERRY, F. J. 1971 Flow field produced by trailing vortices in the vicinity of the ground. *AIAA J.* **9**, 1659–1660.

HEDEGAARD, J. B. 1985 Wave generated ripples and resulting sediment transport in waves. *Series Paper n.* 36. Inst. of Hydrodynamic and Hydraulic Engng, Technical University of Denmark.

HINO, M., SAWAMOTO, M. & TAKASU, S. 1976 Experiments on transition to turbulence in an oscillatory pipe flow. *J. Fluid Mech.* **75**, 193–207.

IKEDA, S., KIZAKI, S., ISHII, S. & KURIBAYASHI, S. 1989 Flow near sand ripples and dissipation of wave energy. *Coast. Engng Japan* **32**, 15–36.

LOFQUIST, K. E. B. 1980 Observation of drag on naturally rippled sand beds under oscillatory flows. *Proc. XVII Conf. on Coastal Engng, Sydney, Australia*, pp. 3087–3106. ASCE.

LONGUET-HIGGINS, M. S. 1981 Oscillating flow over steep sand ripples. *J. Fluid Mech.* **107**, 1–35.

LYNE, W. H. 1971 Unsteady viscous flow over wavy wall. *J. Fluid Mech.* **50**, 33–48.

MERKLY, P. & THOMANN, H. 1975 Transition to turbulence in oscillatory pipe flow. *J. Fluid Mech.* **68**, 567–575.

NAKATO, T., LOCHER, F. A., GLOVER, J. R. & KENNEDY, J. F. 1977 Wave entrainment of sediment from rippled beds. *J. Waterways, Port, Coastal & Ocean Engng. Div. ASCE* **103**, (WW1) 83–99.

NIELSEN, P. 1979 Some basic concepts of wave sediment transport. *Series Paper n. 20.* Inst. Hydrodynamics and Hydraulic Engng, Technical University of Denmark.

ORSZAG, S. A. 1971 Numerical simulation of incompressible flows within simple boundaries: accuracy. *J. Fluid Mech.* **49**, 75–112.

RALPH, M. E. 1986 Oscillatory flows in wavy-walled tubes. *J. Fluid Mech.* **168**, 515–540.

RALPH, M. E. 1988 Pressure drop and power dissipation in oscillatory wavy-walled-tube flows. *J. Fluid Mech.* **187**, 573–588.

RINALDO, A. & GIORGINI, A. 1983 A mixed algorithm for the calculation of rapidly varying fluid flows: the impulsively started circular cylinder. *Int. J. Numer. Methods Fluids* **4**, 949–969.

ROACHE, P. J. 1972 *Computational Fluid Dynamics.* Hermosa.

SATO, S., MIMURA, N. & WATANABE, A. 1984 Oscillatory boundary layer flow over a rippled bed. *Proc. XIX Conf. on Coastal Engng, Houston*, pp. 2293–2309. ASCE.

SATO, S., SHIMOSAKO, K. & WATANABE, A. 1987 Measurements of oscillatory turbulent boundary layer flow above ripples with a laser-Doppler velocimeter. *Coast. Engng Japan.* **30**, 89–98.

SLEATH, J. F. A. 1973 A numerical study of the influence of bottom roughness on mass transport by water waves. *Proc. Intl Conf. Numerical Methods in Fluid Dynamics, Southampton.*

SLEATH, J. F. A. 1984 *Sea Bed Mechanics.* Wiley.

SMITH, P. A. & STANSBY, P. K. 1985 Wave-induced bed flows by a Lagrangian vortex scheme. *J. Comput. Phys.* **60**, 489–516.

SMITH, P. A. & STANSBY, P. K. 1988 Impulsively started flow around a circular cylinder by the vortex method. *J. Fluid Mech.* **194**, 45–77.

SOBEY, I. J. 1980 On flow through furrowed channels. Part 1. Calculated flow patterns. *J. Fluid Mech.* **96**, 1–26.

SOBEY, I. J. 1982 Oscillatory flows at intermediate Strouhal number in asymmetric channels. *J. Fluid Mech.* **125**, 359–373.

SOBEY, I. J. 1983 The occurrence of separation in oscillatory flow. *J. Fluid Mech.* **134**, 247–257.

STOKES, G. G. 1851 On the effect of the internal friction of fluids on the motion of pendulums. *Trans. Camb. Phil. Soc.* **9**, 20–21.

SUNAMURA, T. 1980 A laboratory study of offshore transport of sediment and a model for eroding beaches. *Proc. XVII Conf. on Coastal Engng, Houston*, pp. 1051–1070. ASCE.

THOM, A. 1928 An investigation of fluid flow in two-dimensions. *Aero. Res. Counc. R. & M.*, 1194.

TROMANS, P. 1976 The stability of oscillating pipe flow. *Euromech '73: Oscillatory Flows in Ducts, Aix-en-Provence, April 13–15.*

VAN DYKE, M. 1975 *Perturbation Methods in Fluid Mechanics.* Parabolic.

VITTORI, G. 1988 Sulla potenza dissipata da onde di gravità progressive in presenza di ripples. *XXI Congresso di Idraulica e Costruzioni Idrauliche, L'Aquila, 5–8 Sept.*

VITTORI, G. 1989 Non linear viscous oscillatory flow over a wavy wall. *J. Hydraul. Res.* **27**, 267–280.

WALKER, J. D. A. 1978 The boundary layer due to rectilinear vortex. *Proc. R. Soc. Lond.* A **359**, 167–188.